

Weiss, Y., Navon, O., Goldstein, S. L. and Harris, J. W. (2018) Inclusions in diamonds constrain thermo-chemical conditions during Mesozoic metasomatism of the Kaapvaal cratonic mantle. *Earth and Planetary Science Letters*, 491, pp. 134-147. (doi:[10.1016/j.epsl.2018.03.014](https://doi.org/10.1016/j.epsl.2018.03.014))

This is the author's final accepted version.

There may be differences between this version and the published version. You are advised to consult the publisher's version if you wish to cite from it.

<http://eprints.gla.ac.uk/161106/>

Deposited on: 23 April 2018

Enlighten – Research publications by members of the University of Glasgow
<http://eprints.gla.ac.uk>

Thermo-chemical conditions during Mesozoic metasomatism at the southwestern Kaapvaal cratonic mantle

Yaakov Weiss^{1,2*}, Oded Navon², Steven L. Goldstein^{1,3}, Jeff W. Harris⁴

¹ Lamont-Doherty Earth Observatory of Columbia University, Palisades, New York 10964, USA (yweiss@ldeo.columbia.edu)

² The Freddy and Nadine Herrmann Institute of Earth Sciences, The Hebrew University of Jerusalem, Jerusalem 91904, Israel

³ Department of Earth and Environmental Sciences, Columbia University, Palisades, New York 10964, USA

⁴ School of Geographical and Earth Sciences, University of Glasgow, Glasgow, G12 8QQ, UK

Abstract

Fluid/melt inclusions in diamonds, which were encapsulated during a metasomatic event and over a short period of time, are isolated from their surrounding mantle, offering the opportunity to constrain changes in the sub-continental lithospheric mantle (SCLM) that occurred during individual thermo-chemical events, as well as the composition of the fluids involved and their sources. We have analyzed a suite of 8 microinclusion-bearing diamonds from the Group I DeBeers-Pool kimberlites, South Africa, using FTIR, EPMA and LA-ICP-MS. Seven of the diamonds trapped incompatible element enriched saline high density fluids (HDFs), carry peridotitic mineral microinclusions, and interstitial nitrogen almost exclusively in A-centers (Type-IaA IR spectrum). The low-aggregated nitrogen of these diamonds, indicates a short mantle residence times and/or low temperatures. As during and following the Karoo flood basalt volcanism, elevated thermal conditions prevailed in the South African lithosphere, the saline metasomatism must have occurred in proximity to kimberlite eruptions at ~85 Ma. Another diamond encapsulated incompatible element enriched silicic HDFs and exhibits an aggregated

nitrogen Type IaAB spectrum with 25% B-centers, implying formation during an earlier and different metasomatic event that likely relates to the Karoo magmatism ca. 180 Ma.

Thermometry of mineral microinclusions in the diamonds carrying saline HDFs, based on Mg–Fe exchange between garnet–orthopyroxene (Opx)/clinopyroxene (Cpx)/olivine and Opx–Cpx, yield temperatures between 875–1080 °C at 5 GPa. These temperatures overlap with conditions recorded by touching inclusion pairs in diamonds from the DeBeers-Pool kimberlites, which represent the mantle ambient conditions just before eruption, and are altogether lower by 150–250 °C compared to P–T gradients recorded by peridotite xenoliths from the same locality. Oxygen fugacity (fO_2) differs as well. The fO_2 calculated for the saline HDF compositions ($\Delta \log fO_{2(FMQ)} = -2.55$ to -1.43) are higher by about a log unit compared to xenolith fO_2 values at 4–7 GPa. We suggest that enriched saline HDFs mediated the metasomatism that preceded Group I kimberlite eruptions in the southwestern Kaapvaal craton, and that their ‘cold and oxidized’ nature reflects their derivation from a deep subducting slab. This event had little impact on the temperature and redox state of the Kaapvaal lithosphere as a reservoir, however, it likely affected its properties along limited metasomatised veins and noodles. To reconcile the temperature and oxygen fugacity discrepancy between inclusions in diamonds and associated xenoliths, we argue that xenoliths did not equilibrate during the last saline metasomatic event and/or kimberlite eruption. Thus the P–T– fO_2 gradients they record express pre-existing lithospheric conditions that were likely established during the last major thermal event in the Kaapvaal craton (i.e. the Karoo magmatism ca. 180 Ma).

1. Introduction

Constraining thermo-chemical changes in the sub continental lithospheric mantle (SCLM), which influence its density and stability (e.g. Baptiste and Tommasi, 2014; Carlson et al., 2005;

Deen et al., 2006), rheology (e.g. Eaton et al., 2009) and oxidation state (e.g. Luth and Stachel, 2014; Tappe, et al. 2007), is an on-going fundamental challenge in mantle geodynamics. Direct samples of the mantle (xenoliths and xenocrysts) provide information on the timing of such temporal modifications, the depth within the lithosphere where changes take place, and the temperature and chemical/mineralogical modifications that occur during such events (e.g. Lazarov et al., 2009a, 2012; Simon et al., 2007). In most cases fluid-rock interaction during metasomatism is the driving force for alteration, but remnants of the metasomatic agent involved are only rarely observed (i.e. van Achterbergh et al., 2002). The nature of mantle metasomatic fluids must therefore be inferred indirectly, from geochemical proxies or calculated using mineral/melt partition coefficients. Also, the possible chemical overprinting of mantle rocks by multiple alteration/enrichment events over cratonic histories permits debate on whether metasomatism was accomplished by interaction with fluid or melt, and of what type? For example, silicic or carbonatitic, oxidizing or reduced? what are the effects such interactions have on the rock lithologies and chemical compositions? And in addition, what linkages exist between the mantle sources of the fluids/melts involved in metasomatism and regional tectonic episodes?

The SCLM of the southwestern part of the Kaapvaal Craton in South Africa has been studied intensively. Mantle derived xenoliths and xenocrysts from this area document intensive Archean depletion by melting, with up to >40% melt extraction (e.g. Griffin et al., 2003; Kelemen et al., 1998; Pearson et al., 1995), followed by a complex metasomatic history that is related to several tectonic and magmatic events. Archean enrichment in SiO₂, light rare earth elements (LREEs) and large ion lithophile elements (LILE; K, Ba, Ca, Sr) is attributed to hydrous fluids and silicate and carbonatitic melts released from subducting slabs during and after amalgamation of the

Kimberley and Witwatersrand blocks, at ca. 2.9 Ga (e.g. Bell et al., 2005; Shirey et al., 2004; Simon et al., 2007), and until the final stabilization of the craton at ~2.6 Ga (Lazarov et al., 2009a, 2012). During the Proterozoic and early Phanerozoic three phases of metasomatism, thought to be induced by subduction-derived aqueous fluids and/or silicic-carbonatitic melts that formed *in-situ* within a previously metasomatised SCLM, are recorded at 1.9 ± 0.2 Ga, 1.3 ± 0.4 Ga and 0.4 ± 0.12 Ga (e.g. Lazarov et al., 2009a, 2012). The timings of alteration coincide with the Kheis-Magondi orogeny at 1.93–1.89 Ga (Armstrong, 1987), the Namaqua–Natal orogeny at 1.2–1 Ga (Pettersson et al., 2007) and the formation of the Damara belts and their attachment to the craton at ~500 Ma (Gray et al., 2008). ‘Young’ metasomatism, which involved enrichment of the SCLM in high-field-strength elements (HFSE; Ti, Zr, Hf, Nb), LILE and LREE and the formation of pyroxene, phlogopite, amphibole, Fe-Ti Oxides and LIMA (lindsleyite–mathiasite) phases, has been attributed to Mesozoic magmatism (e.g. Giuliani et al., 2014; Simon et al., 2007), of both the Karoo flood basalt event (175–185 Ma, Jourdan et al., 2007) and the eruptions of Group II and Group I kimberlites (mainly at $\sim125\pm10$ and 85 ± 5 Ma, respectively) (Field et al., 2008 and references therein).

Along with the chemical modifications, mantle metasomatism is responsible for thermal perturbations and changes in the oxygen fugacity (fO_2) of the SCLM. Mantle xenoliths and xenocrysts are likely to record changes mainly due to the last metasomatic event, before their sampling and ascent in kimberlitic magmas. For example, xenoliths from the Kaapvaal lithosphere mostly cluster along a temperature-depth calculated geotherm for continental shield regions ($40\text{--}42$ mW/m², e.g. Rudnick, 1999); while thermally perturbed xenoliths from depths greater than 150 km (>5 GPa) are displaced to higher temperatures, away from the general P-T gradient, and are characterized by textural deformation and incompatible element enrichment

(Bell et al., 2003; Boyd and Gurney, 1986). These thermal variations in the Kaapvaal SCLM are interpreted as the result of Cretaceous metasomatism in the time frame between the eruption episodes of Group II and Group I kimberlites (Bell et al., 2003; Griffin et al., 2003; Kobussen et al., 2009). Associated garnet peridotite xenoliths provide evidence for an fO_2 increase during metasomatism, by up to $\sim 2 \Delta \log$ units in the most incompatible element enriched samples from the southwestern province of the Kaapvaal (e.g. Creighton et al., 2009; Woodland and Koch, 2003). Among these, the recorded increase in fO_2 along compositional changes from core to rim in some xenolithic zoned garnets is estimated to take place within <1 Ma of kimberlite eruption (Griffin et al., 1999; McCammon et al., 2001; Berry, et al. 2013). The change in fO_2 , approaches the enstatite+magnesite=forsterite+graphite/diamond+ O_2 (EMOG/D) reaction curve (Eggler and Baker, 1982), suggesting the involvement of oxidized fluid/melt during metasomatism.

Here we focus on the recent metasomatic events that took place at the southwestern Kaapvaal SCLM, prior to, and between, the Mesozoic kimberlite eruption episodes. However rather than investigating the chemical changes of lithospheric rocks and inferring the metasomatic agent involved, we look directly at the fluids and melts responsible for alteration, by analyzing the composition of micrometer-size inclusions in fluid-rich diamonds. We report the major- and trace-element data for a suite of eight such microinclusion-bearing diamonds from the DeBeers-Pool kimberlites (a cluster of four kimberlites in Kimberley, South Africa). These diamonds encapsulate both high-density fluid (HDF) and mineral microinclusions, allowing us to constrain the composition of the metasomatic agent, the nature of the diamond host rock and the thermal and fO_2 conditions during fluid-rock interaction. Combining our data and results on mineral inclusions in monocrystalline diamonds and garnet-bearing peridotite xenoliths from DeBeers-

Pool and related kimberlites in the southwestern Kaapvaal region, we discuss the source and evolution of the metasomatic agent, constrain the timing of alteration and fluid-rich diamond growth and, evaluate the impact of Mesozoic metasomatism and volcanism on the thermal and redox state of the provenance lithosphere.

2. Samples and analytical techniques

A suite of eight diamonds from the DeBeers-Pool kimberlites, South Africa, was selected for the present study. The diamonds have large range in size with weight varying between 14–120 mg. Seven diamonds show cube-like morphology and one (ON-DBP-338) is a coated diamond. The samples vary in color (white-gray-black-green) and carry abundant microinclusions. Three of the diamonds (ON-DBP-330, 335, 337) show a clear distinction between an inner and outer part, characterized with different hue and cathodoluminescence (CL) intensities (Figure 1 and Supplementary Figure S1). Each diamond was laser-cut twice to create a thin slab that was polished on both sides. It was then cleaned ultrasonically in a mixture of HF 60% and HNO₃ 69% for 2 h and washed with ethanol and distilled water before analysis. Electron probe microanalyzer (EPMA), Fourier-transform infrared (FTIR) and laser ablation ICP-MS analyses were performed for collecting data on the nitrogen concentration and aggregation states in the different diamonds, and the major and trace element composition and volatile content of the microinclusions they carry. Full analytical techniques are presented in Supplementary Material – Analytical Methods.

3. Results

3.1. Nitrogen impurities and included material – FTIR spectroscopy

The DeBeers-Pool diamonds carry 0 to 660 ppm nitrogen in their lattice (Table 1), similar to concentrations detected in other South African fluid-rich diamonds (e.g. Izraeli et al., 2001).

Diamond ON-DBP-336 is a Type IIa diamond; this is the first report of a fluid-rich diamond carrying no nitrogen impurities (Supplementary Figure S2). Four diamonds (ON-DBP-330, 335, 337, 338) exhibit pure Type IaA spectrum and carry nitrogen in A-centers solely, while diamond ON-DBP-332 reveals a Type IaAB with 25% of its nitrogen in B-centers. It also has an associated platelet band at 1373 cm^{-1} (Figure 2 and Supplementary Figure S2, Table 1). This difference indicates a longer mantle residence time or higher ambient temperature for ON-DBP-332 (Taylor et al., 1990). Diamonds ON-DBP-331 and ON-DBP-339 are opaque and no IR spectrum could be collected.

Previous studies have shown that both primary mineral microinclusions and HDF microinclusions (including various daughter mineral phases and a residual low-density hydrous solution) contribute to the IR absorbance in fluid-rich diamonds (e.g. Navon et al., 1988; Tomlinson et al., 2006). In diamonds ON-DBP-337, ON-DBP-338 and the outer parts of ON-DBP-330 and ON-DBP-335, HDF microinclusions show the absorbance of water (IR bands center at ~ 3440 and 1650 cm^{-1}), carbonate (~ 1450 , 880 and 750 cm^{-1}) and apatite (~ 1095 , 1060 and 605 cm^{-1}) (Figure 2 and Supplementary Figure S2). The microinclusions are rich in water compared to carbonate, and their calculated carbonate/(carbonate+water) molar ratio (CMF) ranges between 0.12 and 0.22 (Table 2). A small band/shoulder at $\sim 1000\text{ cm}^{-1}$, in some of the spectra collected, is due to the presence of a daughter mica phase in these microinclusions. HDF microinclusions in diamond ON-DBP-332 are different, they show the IR bands of water and strong absorbance due to the daughter mica phase (central peak at $\sim 1000\text{ cm}^{-1}$) and quartz (1092 , ~ 810 and 785 cm^{-1}); carbonate IR bands were not detected in this diamond (Figure 2 and Supplementary Figure 2).

The absorbance caused by pyroxene (multiple peaks in the range between 600-1150 cm^{-1} , Figure 2 and Supplementary Figure S2) is observed in the inner part of diamond ON-DBP-330, but the characteristic peaks are all displaced to higher wavenumbers by 5-12 cm^{-1} . No carbonate or water bands were detected in this part of the diamond, in agreement with EPMA analysis (section 3.2.1.), which revealed only orthopyroxene associated with olivine microinclusions (Figure 1), confirming that the inner zone is mostly free of HDF microinclusions. In diamond ON-DBP-335, the inner part showed strong carbonate absorbance at 1450, 881 and 750 cm^{-1} but no significant water absorbance was detected, indicating the presence of magnesite rather than HDF microinclusions. Peaks at 1080, 983 and 900 cm^{-1} , which are also observed in the inner part of this diamond, can be related to the presence of pyroxene. Absorbance by both a mica phase and magnesite dominate the spectrum collected in the inner part of diamond ON-DBP-336, while olivine absorbance (~995, 956, 891 and 841 cm^{-1}), with no significant mica or carbonate phases, is observed in the outer regions of this diamond. The absence of water bands in the spectra collected in both zones of this diamond indicate a lack of, or very small amount of HDF microinclusions in this specific diamond, in agreement with EPMA analyses (Supplementary Figure S1 and S2, Supplementary Table A, B).

3.2. High-density fluids and mineral microinclusions – major and trace element compositions

Three hundred and forty-seven HDF microinclusions and one hundred and ninety mineral microinclusions were analyzed in the inclusion-rich zones of the eight diamonds from DeBeers-Pool kimberlites (Figure 1, 3 and Supplementary Figure S1). Seven of these diamonds (ON-DBP-330, 331, 335-339) are rich in saline HDFs; among those, five carry mineral microinclusions: olivine (Ol), orthopyroxene (Opx), clinopyroxene (Cpx), garnet (Grt), phlogopite (Phl) and magnesite (Mgs) were identified, (Table 2). The microinclusions in the

eighth diamond, ON-DBP-332, contains only silicic HDF. In general, all HDFs have elevated concentrations of incompatible elements relative to primitive mantle (PM), with the most incompatible elements (Cs–Pr) reaching levels of a few hundred to a few thousand times the PM values (Figure 4). Variations between individual diamonds, and between saline and silicic HDFs, are described below. The average major element composition of the HDFs in each diamond and the minerals are presented in Table 2 and 3, respectively, with individual microinclusion analyses tabulated in Supplementary Table A and B; trace element analyses are presented in Supplementary Table C.

3.2.1. Mineral inclusions

Mineral microinclusions were found in five of the seven diamonds carrying saline HDFs. In backscattered-electron imaging, these inclusions appear similar in shape to HDF microinclusions and are comparable in size, but their EPMA analysis totals are on average higher (Supplementary Table B). Mixing between mineral and HDF occur in some microinclusions (Figure 3a). The analyzed mineral microinclusions are all of the peridotite paragenesis and always found in association with saline HDFs, but different assemblages are observed, for example, Ol, Ol+Opx, Ol+Opx+Grt, Ol+Opx+Phl+Mgs and Cpx+Mgs (Table 2). Olivine and orthopyroxene are the most abundant mineral microinclusions in the analyzed DeBeers-Pool diamonds, in agreement with the predominance of these two phases in the deep lithosphere of the DeBeers-Pool region (Phillips et al., 2004 and references therein). We used linear regression of the mixing lines between mineral and HDF microinclusions, which are best manifested by oxide (e.g. MgO, SiO₂) vs. Cl wt.% variation diagrams (not shown), to determine the compositions of Ol, Opx, Cpx, Grt and Mgs at Cl=0 wt.% (Table 3). The composition of phlogopite was determined by averaging

204 the 3 inclusions that were found in diamond ON-DBP-336. Below, the compositional variability
 205 of HDF-free mineral phases is described.

206 The Mg# ($100 \times \text{Mg}/(\text{Mg} + \text{Fe})$ molar ratio) of olivine microinclusions is 93.0 ± 0.2 (1 SE on the
 207 regression intercept at Cl=0 wt.%) while that of orthopyroxene is 93.5 ± 0.6 , typical for Kaapvaal
 208 craton mantle peridotites (e.g. Lazarov et al., 2009a). Orthopyroxene microinclusions have
 209 0.4 ± 0.1 wt.% Cr_2O_3 , 0.9 ± 0.1 Al_2O_3 and 0.7 ± 0.2 Na_2O (one inclusion has a relatively high Na_2O
 210 value of 2.9 wt.%); in most cases TiO_2 was not detected. Clinopyroxene microinclusions were
 211 only found in the central part of diamond ON-DBP-335. They have $\text{Mg}\# = 93.2 \pm 0.9$ and Cr#
 212 ($100 \times \text{Cr}/(\text{Cr} + \text{Al})$ molar ratio) of 47.1 ± 2.0 . Both Cr_2O_3 and Na_2O content are elevated, with
 213 values reaching up to 7.0 wt.% and 7.7 wt.%, respectively, indicating a high Na-Cr kosmochlore
 214 component end-member (up to 17 molar%). $\text{Al}_2\text{O}_3 = 3.6 \pm 0.2$ wt.%, $\text{TiO}_2 = 0.4 \pm 0.2$ and K_2O show
 215 minor amounts (0.1 ± 0.1 wt.%) in these Cpx inclusions. Garnet inclusions are Cr-pyrope with
 216 $\text{Mg}\# = 83.8 \pm 1.1$, $\text{Cr}\# = 17.6 \pm 0.8$, and $\text{Cr}_2\text{O}_3 = 5.7 \pm 0.3$ wt.% and $\text{CaO} = 3.5 \pm 0.3$ wt.%. They plot in
 217 the harzburgitic depleted subcalcic garnet field of Grütter et al. (2004) and are all classified as
 218 G10 garnets, similar to many subcalcic garnet inclusions in DeBeers-Pool diamonds (Phillips et
 219 al., 2004). An Mg-rich phase was found in two diamonds (ON-DBP-335 and 336), having
 220 $\text{Mg}\# = 95.8 \pm 0.2$, $\text{MgO} = 88.3 \pm 0.6$ wt.%, $\text{FeO} = 6.9 \pm 0.2$ and $\text{CaO} = 1.3 \pm 0.1$. SiO_2 , Al_2O_3 , Cr_2O_3 ,
 221 MnO , TiO_2 , K_2O and Na_2O are all < 1 wt.% each and sum up to ~ 3 wt.%. The detection of peaks
 222 at 1450, 881 and 750 cm^{-1} in the FTIR spectra collected at the inner region of these two
 223 diamonds indicates that this phase is an Mg-rich carbonate phase (i.e. magnesite). Three
 224 inclusions of low-Ti phlogopite were also analyzed in diamond ON-DBP-336, having an average
 225 composition of $\text{Mg}\# = 95 \pm 1$, 12.8 ± 0.9 wt.% Al_2O_3 , 0.9 ± 0.1 wt.% Cr_2O_3 and a Si/Al and

Si/(Al+Cr) (cation ratio) of 3.1 ± 0.4 and 3.0 ± 0.3 , respectively. In addition, small amounts of 0.3 ± 0.1 wt.% Na_2O and 0.2 ± 0.1 wt.% Cl were detected.

The central part of diamond ON-DBP-330 contains olivine and Opx microinclusions but no HDFs (Figure 1, Supplementary Figure 2). We therefore analyzed this part by LA-ICP-MS, with the aim of determining the trace element composition of the peridotite host. However, most of the elements were below the analyses LOD (except K, Sr, Nb, Ba, La and Ce; Supplementary Table C). Thus, we could reach no conclusions about the trace element composition or pattern of these mineral microinclusions.

3.2.2. Saline HDFs

The HDFs in all seven saline diamonds show similar chemical compositions, varying between the saline end-member and the carbonatitic end-member when projected on a $\text{SiO}_2+\text{Al}_2\text{O}_3$, $\text{CaO}+\text{MgO}+\text{FeO}$ and $\text{Na}_2\text{O}+\text{K}_2\text{O}$ ternary diagram (Figure 3b). On a carbonate- and water-free basis, the average saline fluid is primarily rich in Cl (36.2 ± 5.6 ($1\sigma=\text{STDEV}$) wt.%), K_2O (27.6 ± 7.5 wt.%) and Na_2O (22.3 ± 7.8 wt.%). Other major oxides make up about 22 wt.% altogether: $\text{SiO}_2=2.0\pm1.4$, $\text{CaO}=8.4\pm3.8$, $\text{MgO}=2.3\pm2.0$, $\text{FeO}=5.7\pm3.2$, $\text{BaO}=1.6\pm2.5$, $\text{Al}_2\text{O}_3=1.0\pm0.9$, $\text{P}_2\text{O}_5=0.7\pm0.9$ and $\text{TiO}_2=0.4\pm0.7$ wt.% (as these saline fluids carry Cl^- as a major anion, the total Cl+oxides sum up to >100% due to excess calculated oxygen). The molar proportions of carbonate in the HDF can be estimated assuming cations with positive charge in the fluid are balanced by either carbonate, chloride, phosphate or silicate ions, which then gives $\text{CO}_3=(\text{Mg}+\text{Fe})/2+\text{Ca}+\text{Ba}+(\text{Na}+\text{K}-\text{Al}-\text{Cl})/2-5\text{P}/3$ (Klein-BenDavid et al., 2009). Once the CO_2 is calculated, the water content is determined based on the FTIR CMF ratio (Table 2). When both water and carbonate are included and the total is re-normalized to 100% by weight, the saline HDFs have an average molar proportion of

249 $\text{Si}_{0.7}\text{Ti}_{0.1}\text{Al}_{0.4}\text{Fe}_{1.6}\text{Mg}_{1.1}\text{Ca}_{3.0}\text{Ba}_{0.2}\text{Na}_{14.2}\text{K}_{11.6}\text{P}_{0.2}\text{Cl}_{20.2}(\text{CO}_2)_{6.8}(\text{H}_2\text{O})_{40.1}$. Assuming that all K and
 250 part of the Na are associated with the Cl, the chlorides make up 48% of the saline HDF by
 251 weight (31% KCl and 17% NaCl), H_2O and CO_2 make up 26 and 11 wt.%, respectively, and the
 252 rest (15 wt.%) is taken by oxides bound in carbonates, silicates and phosphates.

253 The major element composition of the saline HDFs show intra- and inter-diamond relationships.
 254 In all diamonds K_2O and Na_2O show a negative correlation (Figure 3c), $\text{K}_2\text{O}+\text{Na}_2\text{O}$ exhibit a
 255 clear positive correlation with Cl and the $\text{Cl}/(\text{Cl}+\text{K}+\text{Na})$ increase with increasing $\text{K}/(\text{K}+\text{Na})$.
 256 MgO correlate negatively with Cl, as do FeO and CaO but with a wider scatter. In addition, in
 257 diamond ON-DBP-335 CaO and P_2O_5 correlates positively and in ON-DBP-330 SiO_2 correlates
 258 negatively with Cl. The inner and outer zones of diamond ON-DBP-337 (Supplementary Figure
 259 S1) show slightly different saline compositions, that is, HDF microinclusions in the outer zone
 260 have on average higher MgO , FeO , CaO , BaO and K_2O , and lower Na_2O and Cl. The molar
 261 $(\text{K}+\text{Na})/\text{Cl}$ ratio in diamonds ON-DBP-338 and 337 varies between 1.01 ± 0.09 (1σ) and
 262 1.24 ± 0.09 , respectively, while it increases up to $(\text{K}+\text{Na})/\text{Cl}=1.33\pm0.12$, 1.37 ± 0.17 and 1.55 ± 0.31
 263 in diamonds ON-DBP-336, 335 and 339, respectively. These variations to higher $(\text{K}+\text{Na})/\text{Cl}$
 264 values correlate with a general increase of MgO , SiO_2 and Na_2O of the HDF microinclusions in
 265 the different diamonds (Figure 3d-f). In addition, CaO , Al_2O_3 and P_2O_3 also increase to some
 266 extent with increasing $(\text{K}+\text{Na})/\text{Cl}$ (not shown). Consequently the calculated molar CO_2 contents
 267 of the HDFs increase by 39%, from $\text{CO}_2=11.1$ wt.% in diamond ON-DBP-338 to $\text{CO}_2=18.3$
 268 wt.% in diamond ON-DBP-339 (Table 2). This increase in CO_2 correlates with increase in
 269 $(\text{K}+\text{Na})/\text{Cl}$ and with increase in the Mg# of the HDFs. We note that the variations in the saline
 270 HDFs, towards somewhat more carbonatitic compositions, appear between diamonds where no
 271 mineral microinclusions were found (i.e. ON-DBP-337 and ON-DBP-338) and diamonds

containing both HDFs and mineral microinclusions (e.g. ON-DBP-336 and ON-DBP-339), and likely represent increasing fluid-rock interaction.

The trace element compositions of the two diamonds where only saline HDF microinclusions were found (ON-DBP-337 and 338) are very similar (Figure 4a). They have high alkalis (K, Rb and Cs), Ba and LREEs compared to Th, U, Nb and Ta levels, and are characterized by conspicuous Ti, Zr, Hf and Y negative anomalies. Variations from these patterns are observed in diamonds where HDF microinclusions reside within an outer growth zone, apparently separated from the mineral microinclusions in an inner part (i.e. diamond ON-DBP-330 and 335), as well as in diamonds containing a mixture of HDF and mineral microinclusions (ON-DBP-331 and 339) (Figure 1, Figure 4 and Supplementary Figure S1). In these diamonds the differences in enrichment between the most incompatible elements (Th, U, Nb and Ta compared to the alkalis, Ba and LREEs) are reduced, as well as the magnitude of the negative anomalies of Ti, Zr, Hf and Y. These compositional changes are manifested as correlative variations between trace elements ratios and the average amount of Cl and MgO (and carbonate), which correlate negatively in the saline HDFs (Figure 5). In general, with decreasing Cl and increasing MgO, the La/Pr ratio increases and Eu/Sm and Ba/Nb ratios decrease; Sr/Rb, Th/Rb and Zr/Hf ratios increase and Eu/Ti ratio decrease, due to higher amounts of Sr, Th, Zr and Ti. There are some outliers for the different trace element ratios, but these do not change the general trends observed in most diamonds.

3.2.3. Silicic HDFs

The HDF microinclusions in diamond ON-DBP-332 have well defined chemical compositions, close to the silicic end-member in fluid-rich diamonds (Figure 3b). On a carbonate- and water-free basis, its average composition is primarily rich in SiO₂ (48±4.5 (1σ) wt.%) and K₂O

(18.5±1.8 wt.%). Other major oxides make up about 35 wt.% altogether (Table 2). SiO₂ exhibits a negative correlation with CaO and P₂O₅. Carbonate absorbance was not detected by FTIR analyses in this diamond (Supplementary Figure S2) and thus, the CMF ratio of the included HDFs could not be determined, nor could the molar proportions of water and carbonate be estimated.

The trace element compositions of the silicic HDFs are comparable to the saline fluids in diamond ON-DBP-337 and 338, however a few key discrepancies exist (Figure 4d). Normalized to primitive mantle values, Th, U and Ba in the silicic fluids are similarly enriched and are elevated compared to the alkalis (K, Rb and Cs). Zr and Hf show positive anomalies compared to elements of similar compatibility during mantle melting, in contrast to the DeBeers-Pool saline HDFs, while the negative anomaly of Ti is relatively small. Ta and Nb show comparable depletion compared to LREEs in both silicic and saline compositions.

3.3. Thermometry, barometry and oxygen fugacity

Temperature conditions during saline metasomatism and fluid-rich diamond formation were calculated using the composition of HDF-free peridotitic mineral microinclusion in the saline HDF-bearing diamonds (Table 3). Equilibrium temperatures were determined with preset pressures between 3-8 GPa using the two-pyroxene thermometer (Brey and Köhler, 1990) and the Mg–Fe exchange thermometers between garnet–clinopyroxene (Krogh, 2000), garnet–olivine (O'Neill and Wood, 1979) and garnet–orthopyroxene (Harley, 1984; Nimis and Grütter, 2010). Pressure conditions were calculated for a 40 mW/m² geothermal gradient (at 3-8 GPa) using various barometers: Al in orthopyroxene (Macgregor, 1974), Cr in clinopyroxene (Nimis and Taylor, 2000) and the garnet-orthopyroxene barometer (Nickel and Green, 1985) with modified Mg-Tschermaks according to (Taylor, 1998). Results are presented in Table 3.

Below the graphite-diamond stability line the different thermometers and barometers define a slanted rhomb shape (Figure 6a), varying over ~500 °C between 4–8 GPa, as the possible temperature conditions for saline metasomatism and the formation of the DeBeers-Pool diamonds that carry saline HDF microinclusions. However at any given pressure the variation in temperature is ~200 °C, so that, for example at 5 GPa, the possible range of temperature is between 875–1080 °C and at 6 GPa lies between 930–1155 °C. Mineral microinclusions of both peridotite and eclogite lithologies in diamonds carrying saline HDFs from the neighboring Koffiefontein kimberlite suggest similar temperature and pressure conditions (Izraeli et al., 2004). In addition, the saline HDFs-bearing diamonds from the two localities (DeBeers-Pool and Koffiefontein) carry nitrogen almost exclusively in A-centers (Table 1 and Supplementary Figure S2; (Izraeli et al., 2004)), indicating formation temperatures of less than 1200 °C (Taylor et al., 1990).

Oxygen fugacities (fO_2) for the saline HDFs were calculated using the mole fraction of CO_2 (X_{CO_2}) in the HDFs (Table 2) and over the range of temperature and pressure presented in Figure 6a, using the calibration of Stagno and Frost (2010) for melt fO_2 in a Ca-bearing peridotite system. The calculated range of $\log fO_2$ for saline HDFs between 4.5–7 GPa, relative to the FMQ buffer, is $\Delta \log fO_{2(FMQ)} = -2.55$ to -1.43 , but the variation at a given pressure is <0.37 $\Delta \log$ units (Figure 6b). These fO_2 values plot mostly along the stability of carbonate-bearing melts having $X_{CO_2}=0.1$ -0.2 between 4 to 5.5 GPa, and $X_{CO_2}=0.1$ -0.4 between 5.5 to 7 GPa (Stagno and Frost, 2010).

4. Discussion

4.1. High-density fluids (HDFs) in DeBeers-Pool diamonds – mantle source, lithospheric host rock and fluid evolution.

341 The chemical compositions of HDF microinclusions in fluid-rich diamonds reflect the various
342 mantle sources of deep mantle metasomatic fluids, which impact the lithosphere and form
343 diamonds. Investigations of the nature of HDFs trapped in fluid-rich diamonds have revealed
344 four compositional end-members globally: saline HDFs that carry mostly K, Na, Cl and water
345 with some carbonates and silicates; high-Mg carbonatitic HDFs characterized by high MgO and
346 carbonate, and low silica, alumina and water; and a continuous array between silicic and low-Mg
347 carbonatitic HDFs with varying amounts of silicates, carbonates and water (e.g. Klein-BenDavid
348 et al., 2009; Navon et al., 1988; Skuzovatov et al., 2016; Smith et al., 2012; Tomlinson et al.,
349 2006; Weiss et al., 2009). Within this framework, Weiss et al. (2015) reported the first
350 conclusive trace-element (i.e. strong and correlative positive anomalies of Eu and Sr) and Sr
351 isotope evidence for seawater-altered subducting slabs as the source of saline HDFs in a set of
352 diamonds from the Northwest Territories, Canada. Saline HDFs in the analyzed DeBeers-Pool
353 diamonds are not characterized with pronounced positive anomalies of Eu and Sr; in most cases
354 they show small positive or no anomalies for Sr and $Eu/Sm < 1$ (Figure 4, 5g). These features by
355 themselves do not require an explicit relationship to recycled oceanic crust. However, the
356 thermal conditions of saline metasomatism in the Kaapvaal SCLM, as determined by
357 geothermobarometry of non-touching mineral microinclusions in the DeBeers-Pool diamonds,
358 reflect the interaction of low temperature saline HDFs with lithospheric rocks (Figure 6a; see
359 section 4.3. below for details and discussion). In addition, the redox states of these saline HDFs
360 are higher compared to the local SCLM, and approach the EMOD reaction curve (Figure 6b).
361 These two lines of evidence indicate that the saline metasomatic agent that altered the
362 southwestern Kaapvaal SCLM were ‘cold and oxidized’ in nature, and could not originate from
363 the ambient lithosphere nor from the underlying ‘hotter’ asthenosphere. We therefore suggest

that the saline HDFs in DeBeers-Pool diamonds are linked to a subducting slab, feasibly through a relationship to early Mesozoic flat-plate subduction under the southwestern margin of Gondwanaland (Lock, 1980).

Weiss et al. (2015) showed a chemical evolutionary trend indicating that silicic HDFs in diamonds from the Northwest Territories formed through fluid-rock interaction of parental saline fluids with eclogitic lithologies in the lithospheric mantle. In the case of the DeBeers-Pool diamonds that were analyzed for the present study, we preclude a direct relationship between the saline and silicic HDFs on the basis of differences between the nitrogen aggregation states of their host diamonds (Figure 2 and Supplementary Figure S2), which translate to differences in time of metasomatism and diamond formation (Section 4.2.). In addition, the lack of mineral microinclusions in diamond ON-DBP-332 does not allow a direct link between the silicic HDFs in this diamond and an eclogite. However, the high silica content of these HDFs (48 ± 4.5 wt.%; Table 2) is consistent with the composition of near-solidus silicic melts/fluids in equilibrium with eclogite (Hammouda 2003; Kessel, et al. 2005), rather than peridotite (e.g. Kessel, et al. 2015). Such compositional HDF-lithology relationship is also supported by the finding of omphacitic pyroxene in association with silicic-to-low Mg carbonatitic HDFs in diamonds from Canada, Guinea and Siberia (Klein-BenDavid et al., 2009; Tomlinson et al., 2006; Weiss et al., 2009; Weiss et al., 2015).

Saline HDFs in DeBeers-Pool diamonds invaded lithospheric peridotite, based on their microinclusions of olivine, orthopyroxene and Cr-pyrope. The appearance of associated magnesite, phlogopite and kosmochlor-bearing diopside microinclusions in the inner part of diamonds ON-DBP-335 and ON-DBP-336 (Supplementary Figure S1) indicate that this lithosphere was previously altered, likely by enriched Na-bearing carbonatite melt (Ikehata and

Arai, 2004). Interaction between saline HDFs and carbonated-peridotite potentially leads to melting and formation of high-Mg carbonatitic HDFs (Weiss et al., 2009; Weiss et al., 2015). Indeed, the possible P-T conditions for saline metasomatism intersect the lherzolite+H₂O±CO₂ solidus (Figure 6a). However, high-Mg carbonatite compositions were not found as HDF microinclusions in DeBeers-Pool diamonds that were analyzed in the present study, nor in fluid-rich diamonds from the neighboring Koffiefontein kimberlite (Izraeli et al., 2001). Mineral inclusions in monocrystalline diamonds from DeBeers-Pool, Koffiefontein and Jagersfontein (Rickard et al., 1989; Phillips et al., 2004; Tappert et al., 2005) indicate that the local peridotite SCLM is dominated by harzburgite lithology, and the P-T conditions of saline metasomatism does not intersect the harzburgite+H₂O+CO₂ solidus (Figure 6a). We therefore suggest that the refractory nature of harzburgite in the southwestern Kaapvaal SCLM, although containing carbonate metasomes, prevented melting and formation of high-Mg carbonatite during saline metasomatism, and that such interaction is reflected by moderate increases of SiO₂, MgO and Na₂O and decreases of Cl in the saline HDFs (Figure 3c-f and 5a). Increasing fluid-rock interaction also led to higher La/Pr, Sr/Rb, Th/Rb and Zr/Hf ratios and lower Eu/Sm, Eu/Ti and Ba/Nb ratios as the fluid evolved (Figure 5), and diamonds could form by isochemical precipitation (Stachel and Luth 2015) or redox processes (Jacob, et al. 2014) due to strong disequilibrium between saline HDFs and the local SCLM (Figure 6).

4.2. Timing of metasomatism and fluid-rich diamond formation.

The overall absence of large silicate and sulfide inclusions in fluid-rich diamonds does not allow for their absolute age determination, i.e. the age of the metasomatic event in which they formed. Therefore, temporal information is commonly drawn from the kinetics of nitrogen aggregation in the diamond lattice, which is a function of the diamond ‘mantle residence time’ (i.e. from

diamond formation until it ascended with the kimberlite), the diamond ‘mantle residence temperature’ (average temperature over mantle residence time) and the diamond nitrogen concentration (Evans, 1992; Taylor et al., 1990, 1996).

The saline HDF-bearing diamonds from DeBeers-Pool kimberlites show pure Type IaA spectrum (Supplementary Figure S2 and Table 1), with no detectable signals of B-centers or C-centers. Using the kinetics of C- to A-centers and A- to B-centers (Taylor et al., 1990, 1996) the diamond ‘mantle residence time’ can be constrained (Navon, 1999). However, it is hard to resolve the presence of nitrogen centers (C, A or B) when they account to less than 1% of the nitrogen. Figure 7 shows that at the conditions where 99.9% of the nitrogen reside in A-centers, both C- and B-centers are present at levels of <0.1%. Diamonds that carry 70-700 ppm nitrogen and show pure Type IaA spectrum (A-centers>99.9%) can reside only a few million years at 1150 °C, but this time grows up to 1000s of Myr at 1000 °C and to longer than the age of the earth at 900 °C (See also Table 1). Age determinations of Type IaA diamonds should therefore be viewed with caution.

In the case of the saline HDF-bearing diamonds from DeBeers-Pool kimberlites, several lines of evidence suggest their formation in proximity to the kimberlitic eruptions. 1) The compositional similarities of the trapped HDFs in these diamonds suggest they all formed during a single metasomatic event and over a short period in time. 2) The temperature of equilibration of touching inclusion pairs in monocrystalline diamonds from DeBeers-Pool, which allowed chemical exchange and equilibration at depth, represent the final mantle ambient temperatures in which diamonds resided (Phillips et al., 2004); they overlap with possible saline metasomatism conditions between 1000-1150 °C and 4.5-7 GPa (Figure 6a). 3) The Karoo magmatism involved a major increase in the temperature of the South African lithosphere (Bell et al., 2003;

433 Janney et al., 2010), followed by slow adjustment of temperature and low cooling rates (Bedini
434 et al., 2004; Michaut and Jaupart, 2007). These arguments, together with the low-aggregated
435 nature of nitrogen in the saline HDF-bearing diamonds, suggest the timing of their formation is
436 younger than the Karoo flood basalt volcanism at 180 ± 5 Ma (Jourdan et al., 2007). At 1150°C
437 and $<0.1\%$ of both B- and C-centers, the mantle residence time of the saline HDF-bearing
438 diamonds is only a few million years (Figure 7). At 1000°C the estimated residence time is
439 longer (on the order of hundreds of millions of years), but if we allow a higher concentration of
440 C-centers (up to 1%) with less than 0.1% of B-centers, shorter residence times of the order of
441 tens of millions of years are also possible.

442 Diamond ON-DBP-332, carrying silicic HDFs, is a Type IaAB diamond with 25% B-centers
443 (Figure 2). Two scenarios can explain the differences in nitrogen aggregation and HDF
444 compositions between ON-DBP-332 and the saline HDF-bearing diamonds from DeBeers-Pool
445 kimberlites. 1) Assuming all fluid-rich diamonds from DeBeers-Pool formed at a similar
446 timeframe before kimberlite emplacement, then the nitrogen aggregation differences can be
447 explained by a $100\text{--}150^\circ\text{C}$ variation in the diamonds mantle residence temperatures, which
448 translates to a pressure difference of ~ 1 GPa along the $36\text{--}38$ mW/m² geotherms (Figure 6a).
449 While not unreasonable, this scenario restricts diamond formation by saline metasomatism to
450 shallower depth compared to diamond formation by silicic metasomatism. 2) Considering the
451 metasomatic events taking place over a short period of time (as mentioned above), the nitrogen
452 aggregated nature of diamond ON-DBP-332 restricts its formation to an earlier and different
453 metasomatic event than the one responsible for the formation of saline HDF-bearing diamonds.
454 We prefer this scenario as it provides a simple explanation for both the nitrogen and HDF
455 compositional variations within the DeBeers-Pool fluid-rich diamonds, and allows their

formation at similar lithospheric depth. The lack of mineral microinclusions in diamond ON-DBP-332 offers no temperature constraints on its formation. Therefore, the timing of ‘earlier’ silicic metasomatism, based on nitrogen aggregation, is hard to evaluate. However considering a residence temperature of 1170-1180 °C to explain the aggregated nature of nitrogen in this diamond, and the accompanying silicic affinity of HDF microinclusions, a relation to silica-rich melts that invaded the southwestern Kaapvaal SCLM during the Karoo magmatism ca. 180 Ma (Giuliani et al., 2014; Rehfeldt et al., 2008), is plausible.

4.3. Thermal and oxygen fugacity variations during Mesozoic metasomatism at the southwestern Kaapvaal lithosphere.

Thermobarometry and oxythermobarometry of xenoliths and xenocrysts carried by kimberlites allow both the reconstruction of palaeogeotherms (e.g. Griffin et al., 2003; Rudnick, 1999) and oxidation profiles with depth (e.g. Frost and McCammon, 2008; Woodland and Koch, 2003), thus providing direct information on the thermal structure and redox state of the lithosphere of different geographical provenances and at different points in time.

Garnet peridotite xenoliths from Cretaceous Group I kimberlites at the southwestern Kaapvaal craton record temperatures that fall predominantly along a conductive continental geotherm of 40–42 mW/m² (Figure 6a). In comparison, xenoliths from the neighboring Finsch kimberlite, a Group II kimberlite that erupted ~30 Ma prior to Group I kimberlites and is located ~130 km to the northwest, record lower temperatures which plot mainly along a geotherm of 38–40 mW/m². Similarly, garnet xenocrysts carried by Cretaceous Group I kimberlites record higher lithospheric temperatures compared to xenocrysts from Group II kimberlites (Griffin et al., 2003; Kobussen et al., 2009). These temperature differences between lithospheric samples closely related in space and time were argued as indicating a local perturbation from a ‘cratonic-like’ steady state

condition, represented by the P-T gradient of xenoliths from Finsch, to higher thermal gradients, as observed by xenoliths from Group I kimberlites, due to Cretaceous metasomatism and volcanism (Bell et al., 2003; Griffin et al., 2003; Kobussen et al., 2009; Lazarov et al., 2009b). The xenoliths reveal a general decrease in $f\text{O}_2$ with depth (Figure 6b), which results principally from the increase of $\text{Fe}^{3+}/\Sigma\text{Fe}$ in garnet with increasing pressure (Gudmundsson and Wood, 1995; Woodland and Oneill, 1993). On the other hand, Luth and Stachel (2014) modeled the oxidizing effect of fluid-rock interaction on mantle peridotite, and concluded that ppm levels of fluid can potentially shift the $f\text{O}_2$ signature of lithospheric peridotite from very reduced (i.e. the iron-wüstite buffer reaction, IW) to oxidized (EMOD/G) conditions. Consequently, it was suggested that the $f\text{O}_2$ profile of xenoliths from the Kaapvaal Craton (Figure 6b) merely reflects the redox state of the last metasomatic interaction (Luth and Stachel 2014; Stachel and Luth 2015).

The geothermobarometry of non-touching mineral microinclusions in the saline HDF-bearing diamonds from DeBeers-Pool (Figure 6a) constrain the possible thermal conditions during saline metasomatism, which preceded the Cretaceous Group I kimberlite event. These conditions overlap with equilibration temperatures of touching inclusion pairs in monocrystalline diamonds from DeBeers-Pool, and on average are altogether lower by 150–250 °C compared to the observed P-T gradient of peridotite xenoliths from both Group II and Group I kimberlites. A significant temperature difference persists, even when a possible underestimation of ~60 °C is taken into account, due to differences between the garnet-orthopyroxene thermometer (used for the inclusions) and the two-pyroxene thermometer (used for the xenoliths) (Brey and Köhler, 1990; Harley, 1984). If mantle-derived xenoliths from the southwestern Kaapvaal lithosphere record a snapshot of thermal advection during the last event of metasomatism and/or kimberlite

eruption (e.g. Bell et al., 2003), then the P-T conditions of non-touching mineral microinclusions in fluid-rich diamonds, touching inclusion pairs in monocrystalline diamonds, and from the xenoliths, should all plot along a similar P-T gradient; however, this is not the case. To reconcile the temperature discrepancy between inclusions in diamond and xenoliths, we suggest that xenoliths did not equilibrate during the last metasomatic event and/or kimberlite eruption, and that the P-T gradients they record represent older lithospheric conditions. Moreover, we observe a gap between the $f\text{O}_2$ conditions of saline HDFs and peridotitic xenoliths (Figure 6b). It implies that the redox states recorded by peridotitic xenoliths from the southwestern Kaapvaal lithosphere, similar to their P-T gradients, do not represent the interaction with saline HDFs during the last metasomatic event, but rather a reflection of the pre-existing lithospheric $f\text{O}_2$ conditions.

Combining the xenolith data with results for HDF microinclusions and mineral inclusions in diamonds provides a better constraint for the thermal and redox history of the southwestern Kaapvaal lithosphere with respect to Mesozoic metasomatism and volcanism. The last major thermal event in the Kaapvaal craton is the Karoo magmatism ca. 180 Ma, expressed by extensive volcanism of flood basalts and related giant sills and dike swarms over an area of more than $3 \times 10^6 \text{ km}^2$, which includes the entire southern African region (Jourdan et al., 2007). The P-T gradient of xenoliths from the southwestern Kaapvaal lithosphere, along a continental geotherm of $40 \pm 2 \text{ mW/m}^2$ (Figure 6a), and their redox state (Figure 6b), is likely a remnant of this event. Modal metasomatism in dunite and wehrlite xenoliths from DeBeers-Pool (Rehfeldt et al., 2008), U-Pb ages of LIMA mineral and zircon (170-190 Ma) in associated phlogopite and clinopyroxene-rich peridotite xenoliths (Giuliani et al., 2014), as well as the apparent relation between the formation of diamond ON-DBP-332 and the Karoo magmatism (discussed above),

all suggest that the related metasomatism involved silicic melts. The other two volcanic events at the southwestern Kaapvaal craton are the eruption of Group II and Group I kimberlites at 125 ± 10 Ma and 85 ± 5 Ma (Field et al., 2008 and references therein), respectively. Compared to the Karoo magmatism, kimberlitic eruptions are local and of small volume, and likely had limited thermal influence on the lithosphere. This suggestion is supported by the non-touching mineral inclusions in the fluid-rich diamonds, formed in proximity to the kimberlite eruption, and touching inclusions in monocrystalline diamonds, representing equilibration temperatures during the last metasomatic and/or kimberlitic event, which show overlapping temperatures that are lower compared to thermal gradients of peridotitic xenoliths from the same kimberlites (Figure 6a). Likewise, the last metasomatic event by saline HDFs, that preceded Group I kimberlite eruptions, had little impact on the temperature and redox conditions of the Kaapvaal lithosphere as a reservoir. However, it likely affected its properties along limited metasomatised veins and noodles, as indicated by the chemical and redox zoning between core and metasomatised rim in some individual xenolithic garnets from DeBeers-Pool kimberlites (Griffin et al., 1999; McCammon et al., 2001; Berry et al., 2013).

5. Summary and conclusions

The DeBeers-Pool diamonds encapsulate both mineral and high-density fluid (HDF) microinclusions, which help constrain the diamond host rock lithology, the composition of metasomatic agents that impact on this mantle lithology, and the thermal and fO_2 conditions during fluid-rock interaction. Seven of the eight diamonds contains saline HDFs associated with carbonated-peridotite on the basis of their microinclusions of olivine, orthopyroxene, Cr-pyroxene, kosmochlore-bearing diopside, magnesite and phlogopite. Their trace-element patterns show high alkalis (K, Rb and Cs), Ba and LREEs compared to Th, U, Nb and Ta, and are characterized

by Ti, Zr, Hf and Y negative anomalies relative to REEs of similar compatibility. Given the low aggregation of the nitrogen of these diamonds (pure Type-IaA IR spectrum), the compositional similarities of their trapped HDFs, and the timing of the Karoo magmatism which elevated the thermal regime of the South African lithosphere, we argue that saline metasomatism and diamond formation took place in proximity to the Group I kimberlite event (~85 Ma), probably within few million years of eruption.

Another diamond trapped silicic HDFs. Comparison of the silicic HDFs trace-element pattern to those of saline fluids reveals similar levels of Th, U and Ba, which are all elevated compared to alkalis, a smaller negative Ti anomaly, and positive Zr and Hf anomalies. The nitrogen aggregated nature of this diamond (Type IaAB with 25% of the nitrogen in B-centers) restricts its formation to an earlier and different metasomatic event than that responsible for the formation of saline HDF-bearing diamonds. The state of the nitrogen aggregation in this diamond and the silicic nature of the HDF microinclusions suggest a relation to silica-rich melts that invaded the southwestern Kaapvaal SCLM prior to, or during, the Karoo magmatism ca. 180 Ma.

Thermometry and oxythermobarometry for saline metasomatism, based on Mg–Fe exchange between Grt–Opx/Cpx/Ol and Opx–Cpx and the saline HDF compositions, yield temperatures between 875–1080 °C and $\Delta \log fO_{2(FMQ)}$ of -2.0 to -1.7 at 5 GPa. They overlap with temperatures recorded by touching inclusion pairs in diamonds from the DeBeers-Pool kimberlites, which represent the mantle ambient conditions just before eruption, and fO_2 stability of carbonate-bearing melts having a mole fraction of CO_2 between 0.1 and 0.2. These conditions are lower by 150–250 °C and higher by about 1 $\log fO_2$ unit compared to P-T- fO_2 gradients recorded by peridotite xenoliths from the same locality. We suggest that incompatible element enriched saline HDFs mediated the metasomatism that preceded Group I kimberlite eruptions in

the southwestern Kaapvaal craton, and that their ‘cold and oxidized’ nature reflects their derivation from a deep subducting slab. This metasomatic event had little impact on the thermal and redox state of the Kaapvaal lithosphere as a reservoir. However, it likely affected its properties along limited metasomatised veins and noodles, in which diamonds could form by isochemical precipitation or redox processes due to strong disequilibrium between saline HDFs and the local SCLM (Figure 6). To reconcile the temperature and oxygen fugacity discrepancy between inclusions in diamond and xenoliths, we suggest that the xenoliths did not equilibrate during the last saline metasomatic event and/or kimberlite eruption. Thus the P-T- fO_2 gradients recorded by the xenoliths represent pre-existing lithospheric conditions, expressing the last major thermal event in the Kaapvaal craton (i.e the Karoo magmatism ca. 180 Ma).

Acknowledgments

We thank W. L. Griffin and S. Y. O’Ryllie for the use of the LA-ICP-MS at Macquarie University, P. B. Kelemen, T. Stachel and G. P. Brey for discussions, D. Walker for discussions and an informal review, and the Diamond Trading Company (a member of the DeBeers Group of Companies) for the donation of diamonds used in this study. V. Stagno and D. Frost are thanked for their help with the calculation of the oxygen fugacity of the HDFs. YW and SG thanks support from NSF grant EAR13-48045 and EAR17-25323, ON thanks support from the German Israeli Foundation (GIF I-1239-301.8/2014). This is Lamont–Doherty Earth Observatory contribution number (# will be provided at time of proofs).

References

Armstrong, R.A., 1987. Geochronological studies on Archaean and Proterozoic formations of the Foreland of the Namaqua Front and possible correlates on the Kaapvaal craton. Witwatersrand University, Johannesburg., p. 274

594 Ballhaus, C., Berry, R.F., Green, D.H., 1991. High pressure experimental calibration of the
595 olivine-orthopyroxene-spinel oxygen geobarometer: implications for the oxidation state of
596 the upper mantle. *Contributions to Mineralogy and Petrology* 107, 27-40.

597 Baptiste, V., Tommasi, A., 2014. Petrophysical constraints on the seismic properties of the
598 Kaapvaal craton mantle root. *Solid Earth* 5, 45-63.

599 Bedini, R.M., Blichert-Toft, J., Boyet, M., Albarède, F., 2004. Isotopic constraints on the cooling
600 of the continental lithosphere. *Earth and Planetary Science Letters* 223, 99-111.

601 Bell, D.R., Gregoire, M., Grove, T.L., Chatterjee, N., Carlson, R.W., Buseck, P.R., 2005. Silica
602 and volatile-element metasomatism of Archean mantle: a xenolith-scale example from the
603 Kaapvaal Craton. *Contributions to Mineralogy and Petrology* 150, 251-267.

604 Bell, D.R., Schmitz, M.D., Janney, P.E., 2003. Mesozoic thermal evolution of the southern
605 African mantle lithosphere. *Lithos* 71, 273-287.

606 Berry, A.J., Yaxley, G.M., Hanger, B.J., Woodland, A.B., de Jonge, M.D., Howard, D.L.,
607 Paterson, D., Kamenetsky, V.S., 2013. Quantitative mapping of the oxidative effects of
608 mantle metasomatism. *Geology* 41, 683-686.

609 Boyd, F.R., and Gurney, J.J., 1986. Diamonds and the African Lithosphere. *Science* 232, 472-
610 477.

611 Brey, G.P., and Köhler, T., 1990. Geothermobarometry in Four-phase Lherzolites II. New
612 Thermobarometers, and Practical Assessment of Existing Thermobarometers. *Journal of*
613 *Petrology* 31, 1353-1378.

614 Carlson, R.W., Pearson, D.G., James, D.E., 2005. Physical, chemical, and chronological
615 characteristics of continental mantle. *Rev. Geophys.* 43, 24.

616 Chevrot, S., Zhao, L., 2007. Multiscale finite-frequency Rayleigh wave tomography of the
617 Kaapvaal craton. *Geophysical Journal International* 169, 201-215.

618 Creighton, S., Stachel, T., Matveev, S., Hoefler, H., McCammon, C., Luth, R.W., 2009.
619 Oxidation of the Kaapvaal lithospheric mantle driven by metasomatism. *Contributions to*
620 *Mineralogy and Petrology* 157, 491-504.

621 Day, H.W., 2012. A revised diamond-graphite transition curve. *American Mineralogist* 97, 52-
622 62.

623 Deen, T.J., Griffin, W.L., Begg, G., O'Reilly, S.Y., Natapov, L.M., Hronsky, J., 2006. Thermal
624 and compositional structure of the subcontinental lithospheric mantle: Derivation from shear
625 wave seismic tomography. *Geochemistry Geophysics Geosystems* 7.

626 Eaton, D.W., Darbyshire, F., Evans, R.L., Gruetter, H., Jones, A.G., Yuan, X., 2009. The elusive
627 lithosphere-asthenosphere boundary (LAB) beneath cratons. *Lithos* 109, 1-22.

628 Eggler, D.H., Baker, D.R., 1982. Reduced volatiles in the system C-O-H: Implications to mantle
629 melting, fluid formation, and diamond genesis, in: Akimoto, S., Manghnam, M.H. (Eds.),
630 High pressure research in geophysics. Center for Academic Publications, Tokyo, Japan, pp.
631 237-250.

632 Evans, T., 1992. Aggregation of nitrogen in diamond, *The Properties of Natural and Synthetic*
633 *Diamond* Academic Press, London, pp. 259-290.

- 634 Field, M., Stiefenhofer, J., Robey, J., Kurszlaukis, S., 2008. Kimberlite-hosted diamond deposits
635 of southern Africa: A review. *Ore Geology Reviews* 34, 33-75.
- 636 Fouch, M.J., Rondenay, S., 2006. Seismic anisotropy beneath stable continental interiors.
637 *Physics of the Earth and Planetary Interiors* 158, 292-320.
- 638 Frost, D.J., McCammon, C.A., 2008. The redox state of Earth's mantle. *Annual Review of Earth*
639 *and Planetary Sciences* 36, 389-420.
- 640 Giuliani, A., Phillips, D., Maas, R., Woodhead, J.D., Kendrick, M.A., Greig, A., Armstrong,
641 R.A., Chew, D., Kamenetsky, V.S., Fiorentini, M.L., 2014. LIMA U-Pb ages link
642 lithospheric mantle metasomatism to Karoo magmatism beneath the Kimberley region, South
643 Africa. *Earth and Planetary Science Letters* 401, 132-147.
- 644 Gray, D.R., Foster, D.A., Meert, J.G., Goscombe, B.D., Armstrong, R., Trouw, R.A.J., Passchier,
645 C.W., 2008. A Damara orogen perspective on the assembly of southwestern Gondwana.
646 *Geological Society, London, Special Publications* 294, 257-278.
- 647 Griffin, L.W., Shee, R.S., Ryan, G.C., Win, T.T., Wyatt, A.B., 1999. Harzburgite to lherzolite
648 and back again: metasomatic processes in ultramafic xenoliths from the Wesselton
649 kimberlite, Kimberley, South Africa. *Contributions to Mineralogy and Petrology* 134, 232-
650 250.
- 651 Griffin, W.L., O'Reilly, S.Y., Natapov, L.M., Ryan, C.G., 2003. The evolution of lithospheric
652 mantle beneath the Kalahari Craton and its margins. *Lithos* 71, 215-241.
- 653 Grütter, H.S., Gurney, J.J., Menzies, A.H., Winter, F., 2004. An updated classification scheme
654 for mantle-derived garnet, for use by diamond explorers. *Lithos* 77, 841-857.
- 655 Gudmundsson, G., Wood, B.J., 1995. Experimental tests of garnet peridotite oxygen barometry.
656 *Contributions to Mineralogy and Petrology* 119, 56-67.
- 657 Hammouda, T., 2003. High-pressure melting of carbonated eclogite and experimental constraints
658 on carbon recycling and storage in the mantle. *Earth and Planetary Science Letters* 214, 357-
659 368.
- 660 Harley, S.L., 1984. An experimental study of the partitioning of Fe and Mg between garnet and
661 orthopyroxene. *Contributions to Mineralogy and Petrology* 86, 359-373.
- 662 Hasterok, D., Chapman, D.S., 2011. Heat production and geotherms for the continental
663 lithosphere. *Earth and Planetary Science Letters* 307, 59-70.
- 664 Holland, T.J.B., Powell, R., 2011. An improved and extended internally consistent
665 thermodynamic dataset for phases of petrological interest, involving a new equation of state
666 for solids. *Journal of Metamorphic Geology* 29, 333-383.
- 667 Ikehata, K., Arai, S., 2004. Metasomatic formation of kosmochlor-bearing diopside in peridotite
668 xenoliths from North Island, New Zealand. *American Mineralogist* 89, 1396-1404.
- 669 Izraeli, E.S., Harris, J.W., Navon, O., 2001. Brine inclusions in diamonds: a new upper mantle
670 fluid. *Earth and Planetary Science Letters* 187, 323-332.
- 671 Izraeli, E.S., Harris, J.W., Navon, O., 2004. Fluid and mineral inclusions in cloudy diamonds
672 from Koffiefontein, South Africa. *Geochimica et Cosmochimica Acta* 68, 2561-2575.

673 Jacob, D.E., Dobrzhinetskaya, L., Wirth, R., 2014. New insight into polycrystalline diamond
674 genesis from modern nanoanalytical techniques. *Earth-Science Reviews* 136, 21-35.

675 Janney, P.E., Shirey, S.B., Carlson, R.W., Pearson, D.G., Bell, D.R., Le Roex, A.P., Ishikawa,
676 A., Nixon, P.H., Boyd, F.R., 2010. Age, Composition and Thermal Characteristics of South
677 African Off-Craton Mantle Lithosphere: Evidence for a Multi-Stage History. *Journal of*
678 *Petrology* 51, 1849-1890.

679 Jourdan, F., Féraud, G., Bertrand, H., Watkeys, M.K., 2007. From flood basalts to the inception
680 of oceanization: Example from the 40Ar/39Ar high-resolution picture of the Karoo large
681 igneous province. *Geochemistry, Geophysics, Geosystems* 8, n/a-n/a.

682 Kelemen, P.B., Hart, S.R., Bernstein, S., 1998. Silica enrichment in the continental upper mantle
683 via melt/rock reaction. *Earth and Planetary Science Letters* 164, 387-406.

684 Kessel, R., Pettke, T., Fumagalli, P., 2015. Melting of metasomatized peridotite at 4–6 GPa and
685 up to 1200 °C: an experimental approach. *Contributions to Mineralogy and Petrology* 169,
686 37.

687 Kessel, R., Ulmer, P., Pettke, T., Schmidt, M.W., Thompson, A.B., 2005. The water–basalt
688 system at 4 to 6 GPa: Phase relations and second critical endpoint in a K-free eclogite at 700
689 to 1400 °C. *Earth and Planetary Science Letters* 237, 873-892.

690 Klein-BenDavid, O., Logvinova, A.M., Schrauder, M., Spetius, Z.V., Weiss, Y., Hauri, E.H.,
691 Kaminsky, F.V., Sobolev, N.V., Navon, O., 2009. High-Mg carbonatitic microinclusions in
692 some Yakutian diamonds—a new type of diamond-forming fluid. *Lithos* 112, Supplement 2,
693 648-659.

694 Kobussen, A.F., Griffin, W.L., O'Reilly, S.Y., 2009. Cretaceous thermo-chemical modification
695 of the Kaapvaal cratonic lithosphere, South Africa. *Lithos* 112, Supplement 2, 886-895.

696 Krogh, R., 2000. The garnet–clinopyroxene Fe²⁺–Mg geothermometer: an updated calibration.
697 *Journal of Metamorphic Geology* 18, 211-219.

698 Lazarov, M., Brey, G.P., Weyer, S., 2009a. Time steps of depletion and enrichment in the
699 Kaapvaal craton as recorded by subcalcic garnets from Finsch (SA). *Earth and Planetary*
700 *Science Letters* 279, 1-10.

701 Lazarov, M., Brey, G.P., Weyer, S., 2012. Evolution of the South African mantle—a case study
702 of garnet peridotites from the Finsch diamond mine (Kaapvaal craton); Part 2: Multiple
703 depletion and re-enrichment processes. *Lithos* 154, 210-223.

704 Lazarov, M., Woodland, A.B., Brey, G.P., 2009b. Thermal state and redox conditions of the
705 Kaapvaal mantle: A study of xenoliths from the Finsch mine, South Africa. *Lithos* 112,
706 Supplement 2, 913-923.

707 Leahy K. and Taylor W. R. (1997) The influence of the Glennie domain deep structure on the
708 diamonds in Saskatchewan kimberlites. *Russ. Geol. Geophys.* 38, 481–491.

709 Lock, B.E., 1980. Flat-plate subduction and the Cape Fold Belt of South Africa. *Geology* 8, 35-
710 39.

711 Luth, R.W., Stachel, T., 2014. The buffering capacity of lithospheric mantle: implications for
712 diamond formation. *Contributions to Mineralogy and Petrology* 168.

713 Luth, R.W., Stachel, T., 2014. The buffering capacity of lithospheric mantle: implications for
714 diamond formation. *Contributions to Mineralogy and Petrology* 168, 1083.

715 Macgregor, I.D., 1974. System MgO–Al₂O₃–SiO₂ – Solubility of Al₂O₃ in enstatite for spinel
716 and garnet peridotite compositions. *American Mineralogist* 59, 110-119.

717 McCammon, C.A., Griffin, W.L., Shee, S.R., O'Neill, H.S.C., 2001. Oxidation during
718 metasomatism in ultramafic xenoliths from the Wesselton kimberlite, South Africa:
719 implications for the survival of diamond. *Contributions to Mineralogy and Petrology* 141,
720 287-296.

721 McDonough, W.F., Sun, S.S., 1995. The composition of the Earth. *Chemical Geology* 120, 223-
722 253.

723 Michaut, C., Jaupart, C., 2007. Secular cooling and thermal structure of continental lithosphere.
724 *Earth and Planetary Science Letters* 257, 83-96.

725 Miensoopust, M., Jones, A.G., Garcia, X., Muller, M., Hamilton, M.P., Spratt, J.E., Evans, R.L.,
726 Evans, S.F., Mountford, A., Fourie, C.J.S., Hutchins, D., Ngwisanyi, T., SAMTEX Team,
727 2006. Lithospheric studies of major Archean cratons and their Proterozoic bounding belts in
728 southern Africa using MT. British Geophysical Association Postgraduate Meeting.
729 Edinburgh. 31 August – 1 September 2006.

730 Navon, O., 1999. Diamond formation in the Earth's mantle, in: Gurney, J.J., Gurney,
731 J.L., Pascoe, M.D., Richardson, S.H. (Ed.), *Proceedings of the 7th International Kimberlite*
732 *Conference* pp. 584-604.

733 Navon, O., Hutcheon, I.D., Rossman, G.R., Wasserburg, G.J., 1988. Lunar planet. *Sci.* XIX, 827-
734 828.

735 Nickel, K.G., Green, D.H., 1985. Empirical geothermobarometry for garnet peridotites and
736 implications for the nature of the lithosphere, kimberlites and diamonds. *Earth and Planetary*
737 *Science Letters* 73, 158-170.

738 Nimis, P., Grütter, H., 2010. Internally consistent geothermometers for garnet peridotites and
739 pyroxenites. *Contributions to Mineralogy and Petrology* 159, 411-427.

740 Nimis, P., Taylor, R.W., 2000. Single clinopyroxene thermobarometry for garnet peridotites. Part
741 I. Calibration and testing of a Cr-in-Cpx barometer and an enstatite-in-Cpx thermometer.
742 *Contributions to Mineralogy and Petrology* 139, 541-554.

743 O'Neill, H.S.C., Wood, B.J., 1979. An experimental study of Fe-Mg partitioning between garnet
744 and olivine and its calibration as a geothermometer. *Contributions to Mineralogy and*
745 *Petrology* 70, 59-70.

746 Pearson, D.G., Carlson, R.W., Shirey, S.B., Boyd, F.R., Nixon, P.H., 1995. Stabilisation of
747 Archaean lithospheric mantle: A ReOs isotope study of peridotite xenoliths from the
748 Kaapvaal craton. *Earth and Planetary Science Letters* 134, 341-357.

749 Pettersson, Å., Cornell, D.H., Moen, H.F.G., Reddy, S., Evans, D., 2007. Ion-probe dating of 1.2
750 Ga collision and crustal architecture in the Namaqua-Natal Province of southern Africa.
751 *Precambrian Research* 158, 79-92.

752 Phillips, D., Harris, J.W., Viljoen, K.S., 2004. Mineral chemistry and thermobarometry of
753 inclusions from De Beers Pool diamonds, Kimberley, South Africa. *Lithos* 77, 155-179.

754 Rehfeldt, T., Foley, S.F., Jacob, D.E., Carlson, R.W., Lowry, D., 2008. Contrasting types of
755 metasomatism in dunite, wehrlite and websterite xenoliths from Kimberley, South Africa.
756 *Geochimica Et Cosmochimica Acta* 72, 5722-5756.

757 Rickard R. S., Harris J. W., Gurney J. J., and Cardoso P. (1989) Mineral inclusions in diamonds
758 from Koffiefontein mine. *Int. Kimberlite Conf.* 4, 1054–1062.

759 Rudnick, R.L., 1999. The thickness and heat production of Archean lithosphere, constraints from
760 xenolith thermobarometry and surface heat flow. *mantle petrology: field observations and*
761 *high-pressure experimentation: a tribute to Francis R. Boyd*, geochemical Soc. spec. 6, 3-12.

762 Shirey, S.B., Richardson, S.H., Harris, J.W., 2004. Integrated models of diamond formation and
763 craton evolution. *Lithos* 77, 923-944.

764 Simon, N.S.C., Carlson, R.W., Pearson, D.G., Davies, G.R., 2007. The origin and evolution of
765 the Kaapvaal cratonic lithospheric mantle. *Journal of Petrology* 48, 589-625.

766 Skuzovatov, S., Zedgenizov, D., Howell, D., Griffin, W.L., 2016. Various growth environments
767 of cloudy diamonds from the Malobotuobia kimberlite field (Siberian craton). *Lithos* 265,
768 96-107.

769 Smith, E.M., Kopylova, M.G., Nowell, G.M., Pearson, D.G., Ryder, J., 2012. Archean mantle
770 fluids preserved in fibrous diamonds from Wawa, Superior craton. *Geology* 40, 1071-1074.

771 Stachel, T., Luth, R.W., 2015. Diamond formation — Where, when and how? *Lithos* 220–223,
772 200-220.

773 Stagno, V., Frost, D.J., 2010. Carbon speciation in the asthenosphere: Experimental
774 measurements of the redox conditions at which carbonate-bearing melts coexist with graphite
775 or diamond in peridotite assemblages. *Earth and Planetary Science Letters* 300, 72-84.

776 Stagno, V., Ojwang, D.O., McCammon, C.A., Frost, D.J., 2013. The oxidation state of the
777 mantle and the extraction of carbon from Earth's interior. *Nature* 493, 84-88.

778 Tappe, S., Foley, S.F., Stracke, A., Romer, R.L., Kjarsgaard, B.A., Heaman, L.M., Joyce, N.,
779 2007. Craton reactivation on the Labrador Sea margins: Ar-40/Ar-39 age and Sr-Nd-Hf-Pb
780 isotope constraints from alkaline and carbonatite intrusives. *Earth and Planetary Science*
781 *Letters* 256, 433-454.

782 Tappert, R., Stachel, T., Harris, J.W., Muehlenbachs, K., Ludwig, T., Brey, G.P., 2005.
783 Diamonds from Jagersfontein (South Africa): messengers from the sublithospheric mantle.
784 *Contributions to Mineralogy and Petrology* 150, 505-522.

785 Taylor, W.R., 1998. An experimental test of some geothermometer and geobarometer
786 formulations for upper mantle peridotites with application to the thermobarometry of fertile
787 Iherzolite and garnet websterite. *Neues Jahrbuch Fur Mineralogie-Abhandlungen* 172, 381-
788 408.

789 Taylor, W.R., Canil, D., Judith Milledge, H., 1996. Kinetics of Ib to IaA nitrogen aggregation in
790 diamond. *Geochimica et Cosmochimica Acta* 60, 4725-4733.

- Taylor, W.R., Jaques, A.L., Ridd, M., 1990. Nitrogen-defect aggregation characteristics of some Australasian diamonds: time-temperature constraints on the source regions of pipe and alluvial diamonds. *American Mineralogist* 75, 1290-1310.
- Tomlinson, E.L., Jones, A.P., Harris, J.W., 2006. Co-existing fluid and silicate inclusions in mantle diamond. *Earth and Planetary Science Letters* 250, 581-595.
- van Achterbergh, E., Griffin, W.L., Ryan, C.G., O'Reilly, S.Y., Pearson, N.J., Kivi, K., Doyle, B.J., 2002. Subduction signature for quenched carbonatites from the deep lithosphere. *Geology* 30, 743-746.
- Weiss, Y., Kessel, R., Griffin, W.L., Kiflawi, I., Klein-BenDavid, O., Bell, D.R., Harris, J.W., Navon, O., 2009. A new model for the evolution of diamond-forming fluids: Evidence from microinclusion-bearing diamonds from Kankan, Guinea. *Lithos* 112, 660-674.
- Weiss, Y., Kiflawi, I., Navon, O., 2010. IR spectroscopy: Quantitative determination of the mineralogy and bulk composition of fluid microinclusions in diamonds. *Chemical Geology* 275, 26-34.
- Weiss, Y., McNeill, J., Pearson, D.G., Nowell, G.M., Ottley, C.J., 2015. Highly saline fluids from a subducting slab as the source for fluid-rich diamonds. *Nature* 524, 339-342.
- Woodland, A.B., Koch, M., 2003. Variation in oxygen fugacity with depth in the upper mantle beneath the Kaapvaal craton, Southern Africa. *Earth and Planetary Science Letters* 214, 295-310.
- Woodland, A.B., O'Neill, H.S.C., 1993. Synthesis and stability of Fe₂₃+Fe₃₂+Si₃O₁₂ garnet and phase relations with Fe₃Al₂Si₃O₁₂-Fe₂₃+Fe₃₂+Si₃O₁₂ solutions. *American Mineralogist* 78, 1002-1015.
- Wyllie, P.J., 1987. Metasomatism and fluid generation in mantle xenoliths. *Mantle Xenoliths*, 609-621.
- Wyllie, P.J., Ryabchikov, I.D., 2000. Volatile Components, Magmas, and Critical Fluids in Upwelling Mantle. *Journal of Petrology* 41, 1195-1206.

Figure captions

Figure 1: Two microinclusion-bearing diamonds from the DeBeers-Pool kimberlites. (a) Diamond ON-DBP-330 showing distinction between a white and translucent inner part and an outer part that is opaque with black-gray-white colors and a sugary texture; the transition

between the two parts is sharp. (b) Cathodoluminescence (CL) image of ON-DBP-330 showing the location and type of microinclusions that were analyzed by EPMA. Olivine and orthopyroxene microinclusions were found only at the inner part of this diamond, while the outer part exclusively contains high-density fluid (HDF) microinclusions of saline composition. (c) Diamond ON-DBP-332. (d) CL image of ON-DBP-332 showing the location of HDF microinclusions of silicic composition. Pits in (a) and (c) were excavated during laser ablation ICP-MS analysis. Additional photomicrograph and CL images of DeBeers-Pool diamonds, that were analyzed in the present study, are presented in Supplementary Figure S1.

Figure 2: Infrared absorbance spectra between 1000-1400 cm^{-1} of: (a) the inner part of diamond ON-DBP-330 and, (b) diamond ON-DBP-332 (same diamonds as in Figure 1). Diamond ON-DBP-330 show nitrogen absorption in A-centers only (A component; main absorbance at 1282 cm^{-1}); ON-DBP-332 has both A- and B-centers, with 25% of the nitrogen in B-centers (B component; main absorbance at 1332 and 1170 cm^{-1}). The spectrum also show absorbance due to nitrogen platelets at 1373 cm^{-1} . Orthopyroxene related absorbance peaks at 1137, 1074, 1045 and 1018 cm^{-1} are observed in the inner part of ON-DBP-330. In ON-DBP-332, the absorbance peaks at 1093 and 997 cm^{-1} are related to quartz and mica phases, respectively. See Supplementary Figure S2 for the full spectra of DeBeers-Pool diamonds analyzed, and text for additional information.

Figure 3: Composition of mineral and HDF microinclusions in diamonds from DeBeers-Pool kimberlites. (a) $\text{SiO}_2 + \text{Al}_2\text{O}_3$ vs. MgO (in wt.%) showing the different mineral microinclusions (Ol-olivine, Opx-orthopyroxene, Cpx-clinopyroxene, Grt-garnet, Phl-phlogopite, Mgs-magnesite) and HDF microinclusions associated with specific DeBeers-Pool diamonds coded by color. Some microinclusions trapped both mineral and HDF indicated as mixing lines. (b)

847 $\text{SiO}_2+\text{Al}_2\text{O}_3-\text{Na}_2\text{O}+\text{K}_2\text{O}-\text{MgO}+\text{FeO}+\text{CaO}$ ternary diagram (in wt.%) showing the HDFs
848 composition in DeBeers-Pool diamonds compared to the global compositional HDF end-
849 members varying between silicic to carbonatitic to saline (shaded area, delineated by average
850 compositions for individual diamonds). (c) K_2O vs. Na_2O (in wt.%) showing the negative
851 correlation between K and Na in saline HDFs in DeBeers-Pool diamonds (silicic HDFs are
852 shown for comparison). (d-f) Na_2O , MgO and SiO_2 (in wt.%) vs. $\text{K}+\text{Na}/\text{Cl}$ (in moles) of saline
853 HDFs in DeBeers-Pool diamonds. These oxides increase (as well as CaO , Al_2O_3 and P_2O_3 to
854 some extent) with increasing $\text{K}+\text{Na}/\text{Cl}$ of the saline HDFs; the change towards somewhat more
855 carbonatitic compositions, appear between diamond where no mineral microinclusions were
856 found and diamonds containing both HDFs and mineral microinclusions.

857 **Figure 4:** Primitive-mantle-normalized incompatible-element patterns of HDFs trapped in
858 DeBeers-Pool diamonds. (a) Diamonds ON-DBP-337 and 338; only HDF microinclusions were
859 found in these diamonds. (b) Diamond ON-DBP-330 and 335; both mineral microinclusions and
860 fluid microinclusions were identified, but they reside in different growth zones of the diamonds.
861 Laser ablation was conducted at the outer part of these two diamonds that carry HDF
862 microinclusions. (c) Diamond ON-DBP-331 and 339; mineral microinclusions and HDF
863 microinclusions reside in the same growth zone in these diamonds. The ablated diamond volume
864 likely contained a mixture of mineral and HDF microinclusions. (d) Diamond ON-DBP-332;
865 only HDF microinclusions were found in this diamond. The average incompatible element
866 pattern of saline HDF of ON-DBP-337 and 338 is plotted for comparison. In all panels (a–d),
867 small symbols – individual LA-ICP-MS analyses, large symbols – HDF average composition in
868 a single diamond. The uncertainties on the values of Yb and Lu are large and they can be
869 regarded as qualitative only. Primitive mantle values are from (McDonough and Sun, 1995).

Figure 5: Relationships between trace element ratios, MgO (in wt.%), the carbonate calculated content (CO₃ in moles) and the Cl amount (in wt.%) in saline HDFs in DeBeers-Pool diamonds. The MgO and carbonate content which represent the carbonatitic end-member component in the saline HDFs correlate negatively with increasing Cl (a-b). With increasing carbonatitic component, La/Pr ratio increases and Eu/Sm and Ba/Nb ratios decrease in the saline HDF, while Sr/Rb, Th/Rb and Zr/Hf ratios increase and Eu/Ti ratio decrease, due to higher Sr, Th, Zr and Ti concentrations (c-i).

Figure 6: Temperature-pressure- fO_2 conditions of peridotite diamond inclusions and xenoliths from the southwestern Kaapvaal craton. (a) The green area represents the possible P-T conditions of saline metasomatism as recorded by non-touching mineral microinclusions in saline HDF-bearing diamonds from DeBeers-Pool (this study), the inset show the different thermometers and barometers which were used to define these conditions (see text for additional information). Also shown are P-T conditions of mineral inclusions in monocrystalline diamonds (touching pairs – red diamonds, non-touching – yellow circles; Phillips et al., 2004); 36–44 mW/m² continental geotherms (black dotted lines; Hasterok and Chapman, 2011); graphite–diamond transition (black solid line; Day, 2012); the solidus for lherzolite+H₂O+CO₂ (green dashed line) and for lherzolite+H₂O (green dotted-dashed line; Wyllie and Ryabchikov, 2000), and the solidus for harzburgite+H₂O+CO₂ (blue dashed line; Wyllie, 1987). (b) fO_2 variations of saline HDFs as a function of pressure (green area), fO_2 was calculated using the possible P-T conditions of mineral microinclusions in (a), the composition of HDFs in the different diamonds (Table 2) and the calibration of Stagno and Frost (2010). Also shown are the iron–wüstite buffer reaction (IW; Ballhaus et al., 1991), graphite–diamond transition reaction and enstatite+magnesite=olivine+graphite/diamond reaction (EMOG/EMOD; Holland and Powell,

2011), and the fO_2 stability of carbonate-bearing melts (blue lines with molar fraction of CO_2 on top; Stagno and Frost, 2010). Xenoliths P-T data (gray diamonds, triangles and circles) are from Woodland and Koch (2003), Creighton et al. (2009) and Lazarov et al. (2009b); their fO_2 values are calculated based on Stagno et al. (2013). The depth of the Kaapvaal lithospheric Keel is estimated based on Rayleigh waves tomography (Chevrot and Zhao, 2007), seismic anisotropy (Fouch and Rondenay, 2006) and electrical-conductivity measurements (Miensoopust et al., 2006).

Figure 7: The aggregation of nitrogen from C-centers (single nitrogen atom) to A-centers (paired nitrogen atoms), and from A-centers to B-centers (aggregates of four nitrogen atoms) as a function of time and temperature, using the calibration of Taylor et al. (1990, 1996). The proportions of nitrogen in A-centers increase with time and temperature as single nitrogen atoms combine to nitrogen pairs (solid red contours), and decrease as nitrogen pairs aggregate to form larger aggregates of four atoms (dashed black contours). Diamonds showing ‘pure’ Type IaA spectrum contain unresolved B-centers or C-centers, that account to less than 1% of the total nitrogen (middle white field). The low-aggregated nature of nitrogen in the DeBeers-Pool diamonds suggest the timing of their formation is younger than the Karoo flood basalt volcanism at 180 ± 5 Ma, which involved a major increase in the temperature of the South African lithosphere. At $1150^\circ C$ and $<0.1\%$ of both B- and C-centers ($A\text{-centers} > 99.9\%$), the mantle residence time of the saline HDF-bearing diamonds, with nitrogen concentrations varying between 70-700 ppm, is only a few million years before kimberlite eruption. At $1000^\circ C$ the estimated residence time for these diamonds is longer (on the order of hundreds of millions of years), but if we allow a higher concentration of C-centers (up to 1%) with less than 0.1% of B-centers, shorter residence times of the order of tens of millions of years are also possible.

916

917

918

919

920

921

922

923

924

925

926

927

928

929

930

931

932 Figures

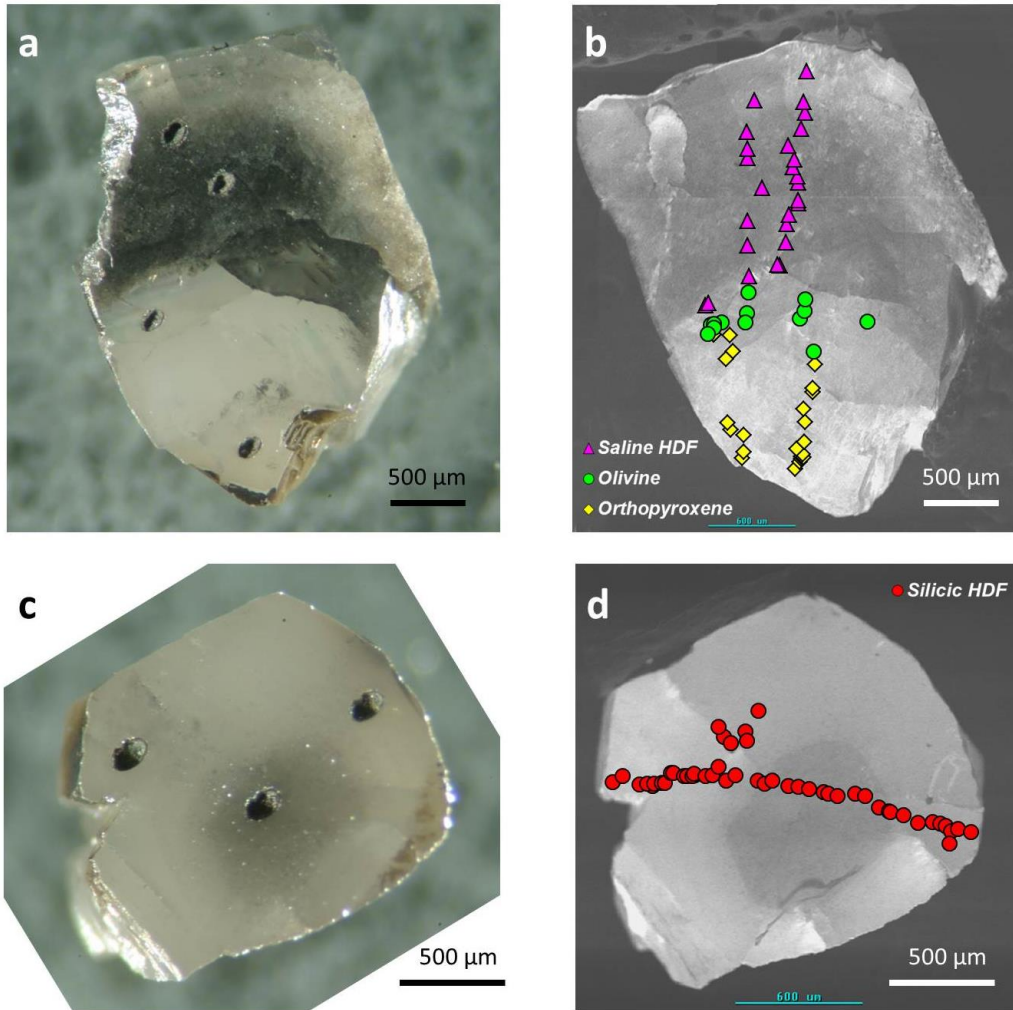


Figure 1: Two microinclusion-bearing diamonds from the DeBeers-Pool kimberlites. (a) Diamond ON-DBP-330 showing distinction between a white and translucent inner part and an outer part that is opaque with black-gray-white colors and a sugary texture; the transition between the two parts is sharp. (b) Cathodoluminescence (CL) image of ON-DBP-330 showing the location and type of microinclusions that were analyzed by EPMA. Olivine and orthopyroxene microinclusions were found only at the inner part of this diamond, while the outer part exclusively contains high-density fluid (HDF) microinclusions of saline composition. (c) Diamond ON-DBP-332. (d) CL image of ON-DBP-332 showing the location of HDF microinclusions of silicic composition. Pits in (a) and (c) were excavated during laser ablation ICP-MS analysis. Additional photomicrograph and CL images of DeBeers-Pool diamonds, that were analyzed in the present study, are presented in Supplementary Figure S1.

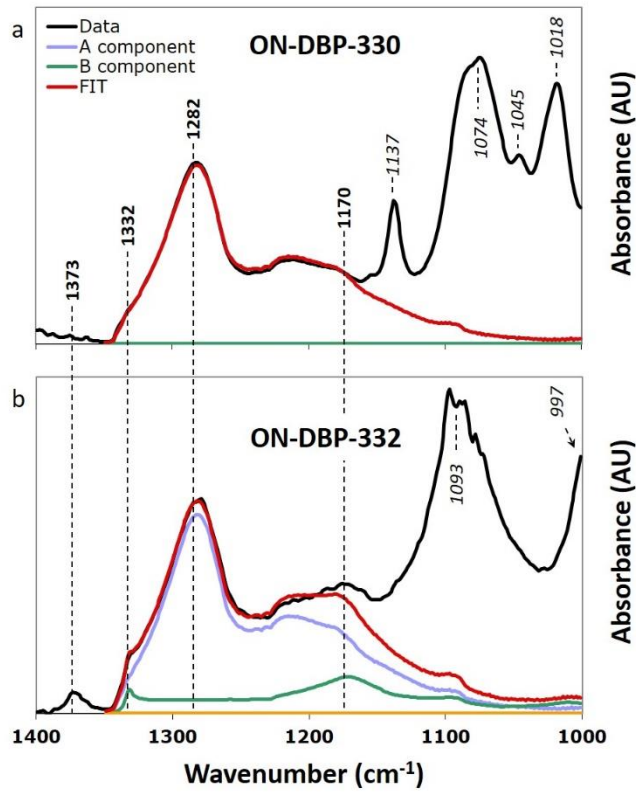


Figure 2: Infrared absorbance spectra between 1000-1400 cm^{-1} of: (a) the inner part of diamond ON-DBP-330 and, (b) diamond ON-DBP-332 (same diamonds as in Figure 1). Diamond ON-DBP-330 show nitrogen absorption in A-centers only (A component; main absorbance at 1282 cm^{-1}); ON-DBP-332 has both A- and B-centers, with 25% of the nitrogen in B-centers (B component; main absorbance at 1332 and 1170 cm^{-1}). The spectrum also show absorbance due to nitrogen platelets at 1373 cm^{-1} . Orthopyroxene related absorbance peaks at 1137, 1074, 1045 and 1018 cm^{-1} are observed in the inner part of ON-DBP-330. In ON-DBP-332, the absorbance peaks at 1093 and 997 cm^{-1} are related to quartz and mica phases, respectively. See Supplementary Figure S2 for the full spectra of DeBeers-Pool diamonds analyzed, and text for additional information.

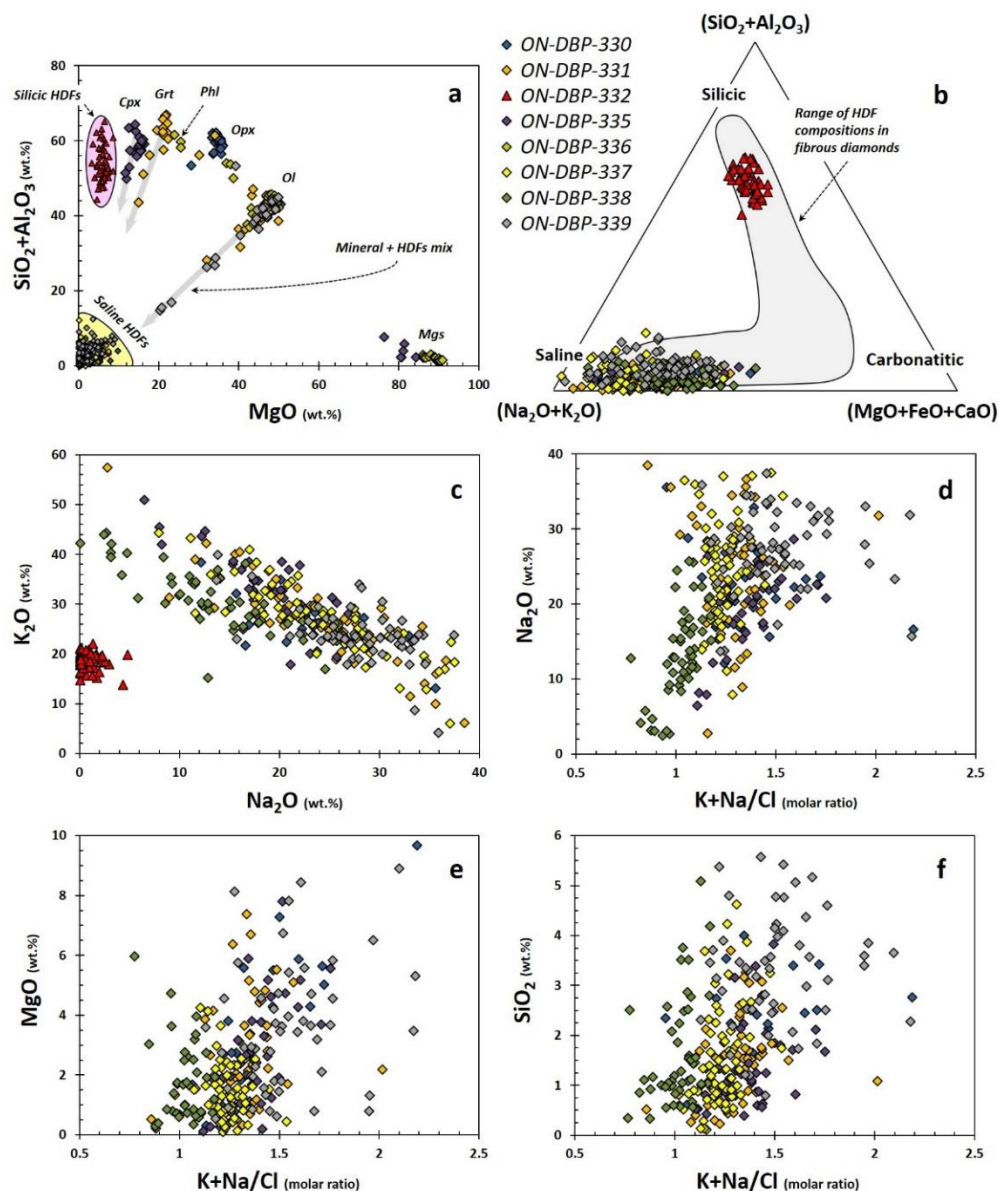


Figure 3: Composition of mineral and HDF microinclusions in diamonds from DeBeers-Pool kimberlites. (a) $\text{SiO}_2 + \text{Al}_2\text{O}_3$ vs. MgO (in wt.%) showing the different mineral microinclusions (Ol-olivine, Opx-orthopyroxene, Cpx-clinopyroxene, Grt-garnet, Phl-phlogopite, Mgs-magnesite) and HDF microinclusions associated with specific DeBeers-Pool diamonds coded by color. Some microinclusions trapped both mineral and HDF indicated as mixing lines. (b) $\text{SiO}_2 + \text{Al}_2\text{O}_3$ – $\text{Na}_2\text{O} + \text{K}_2\text{O}$ – $\text{MgO} + \text{FeO} + \text{CaO}$ ternary diagram (in wt.%) showing the HDFs composition in DeBeers-Pool diamonds compared to the global compositional HDF end-members varying between silicic to carbonatitic to saline (shaded area, delineated by average compositions for individual diamonds). (c) K_2O vs. Na_2O (in wt.%) showing the negative correlation between K and Na in saline HDFs in DeBeers-Pool diamonds (silicic HDFs are shown for comparison). (d-f) Na_2O , MgO and SiO_2 (in wt.%) vs. $\text{K} + \text{Na}/\text{Cl}$ (in moles) of saline HDFs in DeBeers-Pool diamonds. These oxides increase (as well as CaO , Al_2O_3 and P_2O_5 to some extent) with increasing $\text{K} + \text{Na}/\text{Cl}$ of the saline HDFs; the change towards somewhat more carbonatitic compositions, appear between diamond where no mineral microinclusions were found and diamonds containing both HDFs and mineral microinclusions.

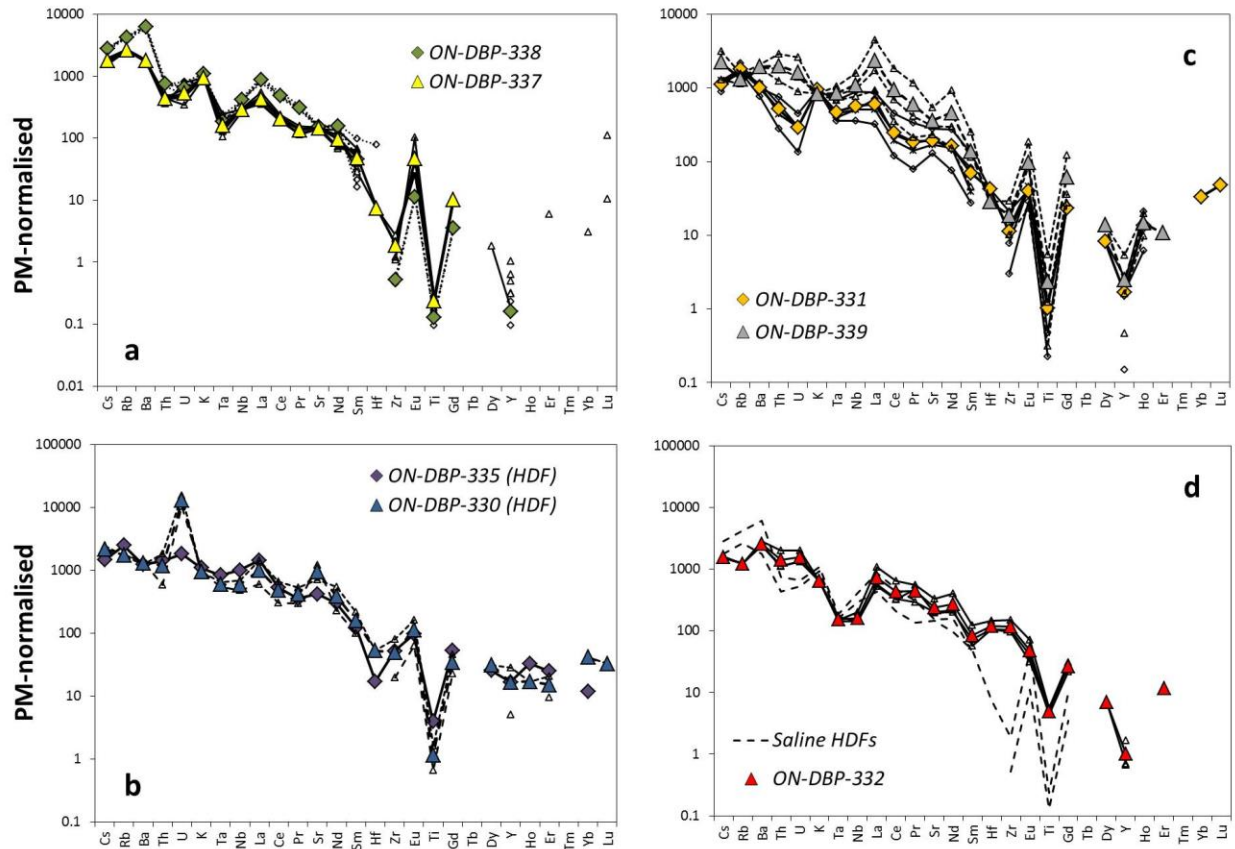


Figure 4: Primitive-mantle-normalized incompatible-element patterns of HDFs trapped in DeBeers-Pool diamonds. (a) Diamonds ON-DBP-337 and 338; only HDF microinclusions were found in these diamonds. (b) Diamond ON-DBP-330 and 335; both mineral microinclusions and fluid microinclusions were identified, but they reside in different growth zones of the diamonds. Laser ablation was conducted at the outer part of these two diamonds that carry HDF microinclusions. (c) Diamond ON-DBP-331 and 339; mineral microinclusions and HDF microinclusions reside in the same growth zone in these diamonds. The ablated diamond volume likely contained a mixture of mineral and HDF microinclusions. (d) Diamond ON-DBP-332; only HDF microinclusions were found in this diamond. The average incompatible element pattern of saline HDF of ON-DBP-337 and 338 is plotted for comparison. In all panels (a–d), small symbols – individual LA-ICP-MS analyses, large symbols – HDF average composition in a single diamond. The uncertainties on the values of Yb and Lu are large and they can be regarded as qualitative only. Primitive mantle values are from (McDonough and Sun, 1995).

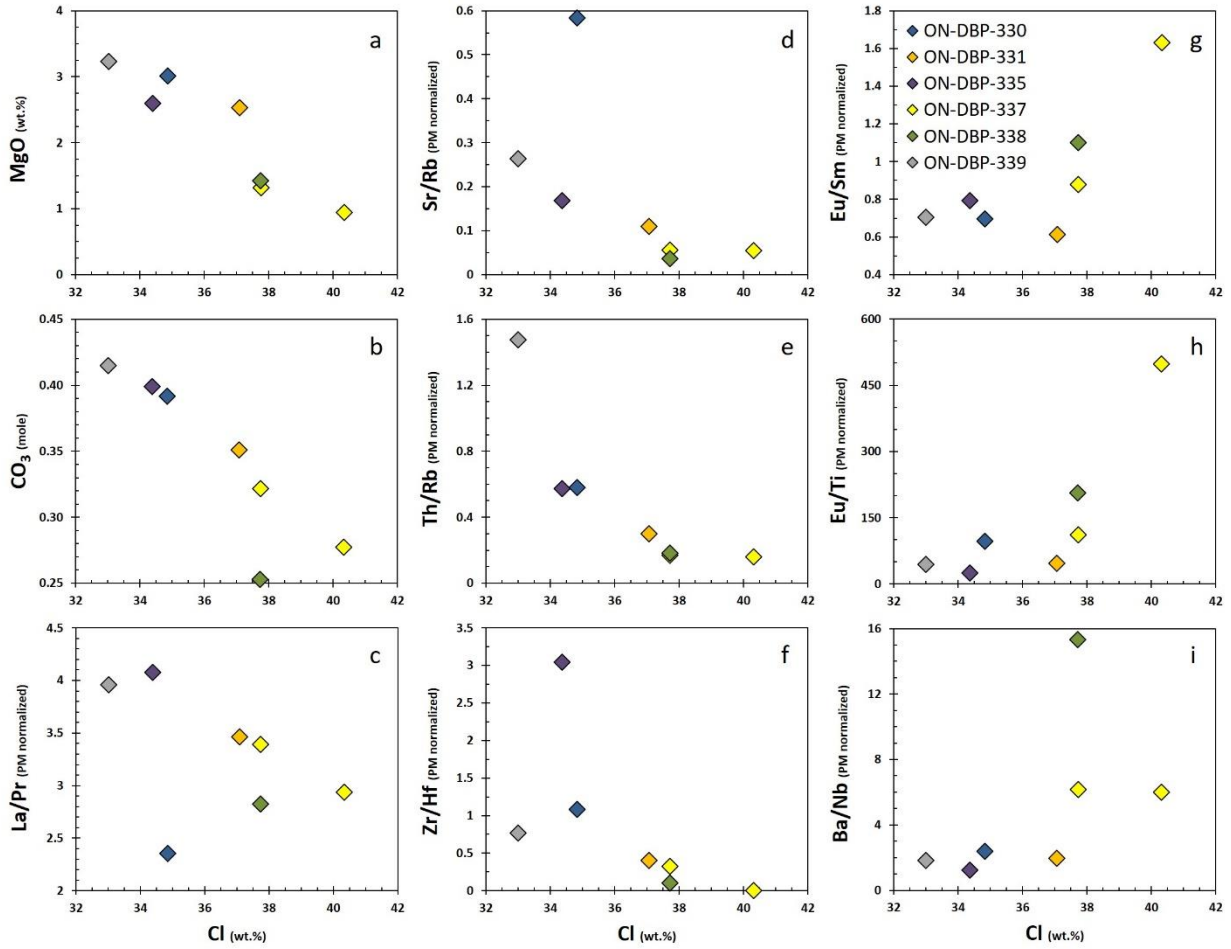


Figure 5: Relationships between trace element ratios, MgO (in wt.%), the carbonate calculated content (CO₃ in moles) and the Cl amount (in wt.%) in saline HDFs in DeBeers-Pool diamonds. The MgO and carbonate content which represent the carbonatitic end-member component in the saline HDFs correlate negatively with increasing Cl (a-b). With increasing carbonatitic component, La/Pr ratio increases and Eu/Sm and Ba/Nb ratios decrease in the saline HDF, while Sr/Rb, Th/Rb and Zr/Hf ratios increase and Eu/Ti ratio decrease, due to higher Sr, Th, Zr and Ti concentrations (c-i).

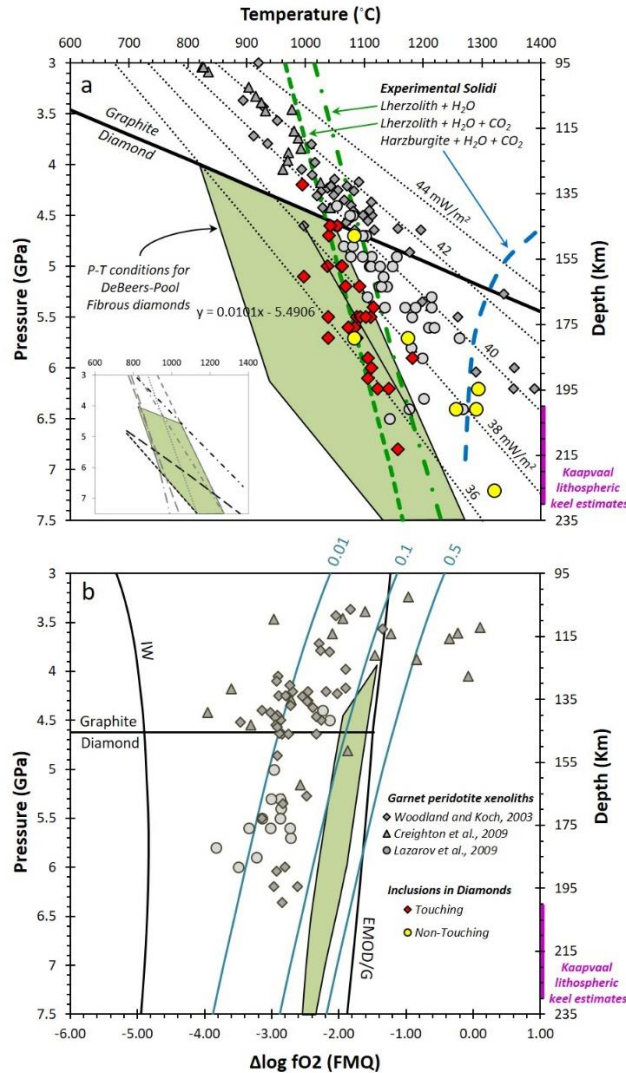


Figure 6: Temperature-pressure- fO_2 conditions of peridotite diamond inclusions and xenoliths from the southwestern Kaapvaal craton. (a) The green area represents the possible P-T conditions of saline metasomatism as recorded by non-touching mineral microinclusions in saline HDF-bearing diamonds from DeBeers-Pool (this study), the inset show the different thermometers and barometers which were used to define these conditions (see text for additional information). Also shown are P-T conditions of mineral inclusions in monocrystalline diamonds (touching pairs – red diamonds, non-touching – yellow circles; Phillips et al., 2004); 36–44 mW/m² continental geotherms (black dotted lines; Hasterok and Chapman, 2011); graphite–diamond transition (black solid line; Day, 2012); the solidus for Lherzolite+ H_2O + CO_2 (green dashed line) and for Lherzolite+ H_2O (green dotted-dashed line; Wyllie and Ryabchikov, 2000), and the solidus for harzburgite+ H_2O + CO_2 (blue dashed line; Wyllie, 1987). (b) fO_2 variations of saline HDFs as a function of pressure (green area), fO_2 was calculated using the possible P-T conditions of mineral microinclusions in (a), the composition of HDFs in the different diamonds (Table 2) and the calibration of Stagno and Frost (2010). Also shown are the iron–wüstite buffer reaction (IW; Ballhaus et al., 1991), graphite–diamond transition reaction and enstatite+magnesite=olivine+graphite/diamond reaction (EMOG/EMOD; Holland and Powell, 2011), and the fO_2 stability of carbonate-bearing melts (blue lines with molar fraction of CO_2 on top; Stagno and Frost, 2010). Xenoliths P-T data (gray diamonds, triangles and circles) are from Woodland and Koch (2003), Creighton et al. (2009) and Lazarov et al. (2009b); their fO_2 values are calculated based on Stagno et al. (2013). The depth of the Kaapvaal lithospheric Keel is estimated based on Rayleigh waves tomography (Chevrot and Zhao, 2007), seismic anisotropy (Fouch and Rondenay, 2006) and electrical-conductivity measurements (Miensoopust et al., 2006).

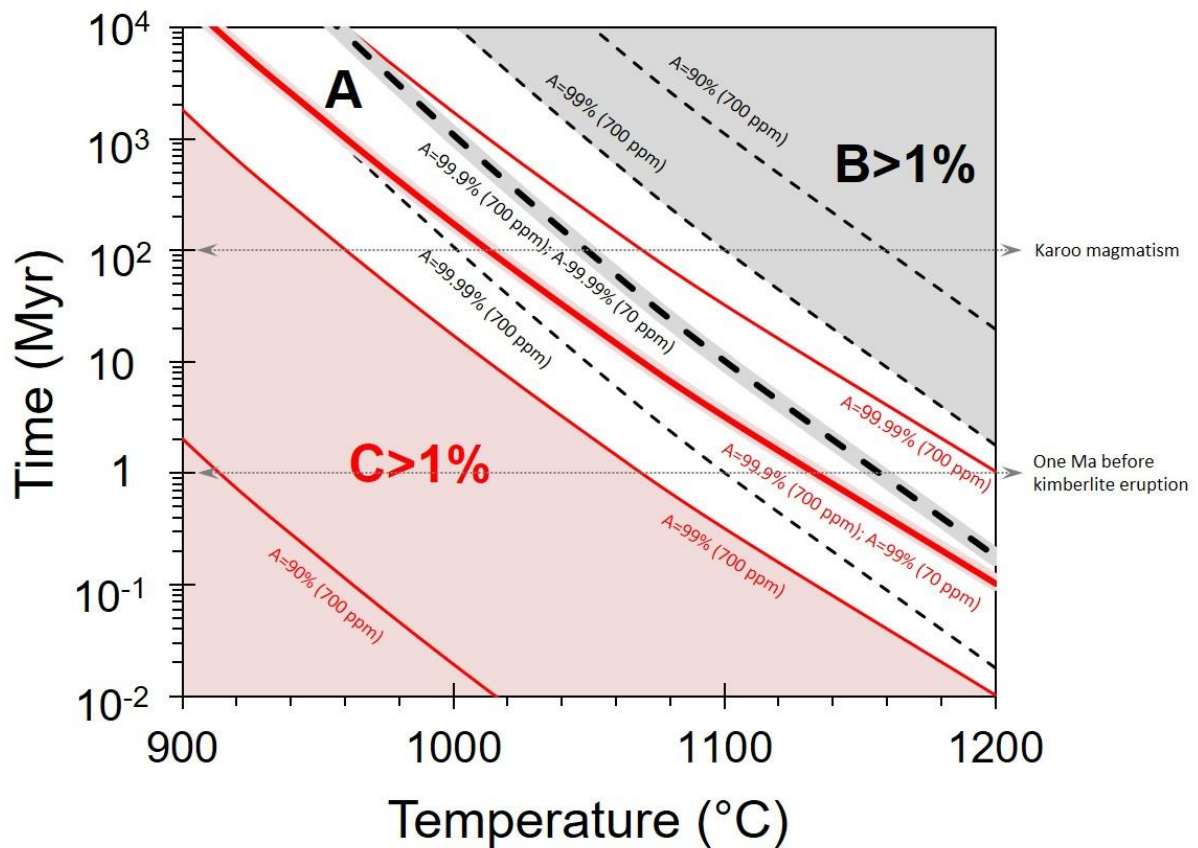


Figure 7: The aggregation of nitrogen from C-centers (single nitrogen atom) to A-centers (paired nitrogen atoms), and from A-centers to B-centers (aggregates of four nitrogen atoms) as a function of time and temperature, using the calibration of Taylor et al. (1990, 1996). The proportions of nitrogen in A-centers increase with time and temperature as single nitrogen atoms combine to nitrogen pairs (solid red contours), and decrease as nitrogen pairs aggregate to form larger aggregates of four atoms (dashed black contours). Diamonds showing ‘pure’ Type IaA spectrum contain unresolved B-centers or C-centers, that account to less than 1% of the total nitrogen (middle white field). The low-aggregated nature of nitrogen in the DeBeers-Pool diamonds suggest the timing of their formation is younger than the Karoo flood basalt volcanism at 180 ± 5 Ma, which involved a major increase in the temperature of the South African lithosphere. At 1150°C and $<0.1\%$ of both B- and C-centers ($A\text{-centers} > 99.9\%$), the mantle residence time of the saline HDF-bearing diamonds, with nitrogen concentrations varying between 70-700 ppm, is only a few million years before kimberlite eruption. At 1000°C the estimated residence time for these diamonds is longer (on the order of hundreds of millions of years), but if we allow a higher concentration of C-centers (up to 1%) with less than 0.1% of B-centers, shorter residence times of the order of tens of millions of years are also possible.

1012 Supplementary Material

1013 Analytical Methods

1014 **Fourier-transform infrared (FTIR) spectroscopy**

1015 Infrared spectra were collected using a Bruker IRscope II microscope coupled to a Nicolet 740
1016 FTIR spectrometer (Globar source, KBr beamsplitter, MCT detector, He–Ne laser) at the
1017 Institute of Earth Sciences, the Hebrew University of Jerusalem, Israel (HUJI). Spectra were
1018 taken in the range of 550–4000 cm^{-1} with resolution of 2 cm^{-1} . Nitrogen concentration and
1019 aggregation states (Table 1) were determined with the DiaMap freeware (Howell et al., 2012),
1020 using the absorption coefficients of A-centers (double substitution of carbon atoms by two
1021 nitrogen atoms, Type IaA spectrum), B-centers (clusters of 4 nitrogen atoms and an atomic
1022 vacancy substituting 5 carbon atoms, Type IaB spectrum) and C-centers (single nitrogen
1023 replacing a carbon atom, Type Ib spectrum) (Boyd et al., 1994, 1995; Kiflawi et al., 1994;
1024 Zaitsev, 2001). Prior to deconvolution, the DiaMap program subtracts the intrinsic diamond
1025 absorption spectrum (Type IIa spectrum) and baseline corrects the raw data automatically (using
1026 a spline fit to the lowest points). The infra-red spectra obtained are complicated by the partial
1027 overlapping absorbances of silicates, carbonates and apatite from the microinclusions (Figure 2
1028 and Supplementary Figure S2). As a consequence, deconvolution of the low-nitrogen IR
1029 absorbance to determine nitrogen concentrations and aggregation states was made more difficult,
1030 in particular resulting in over-estimation mainly of the percentage of nitrogen in the B-centers.
1031 To correct for the over-estimation, we manually set the spectral fitting range of the DiaMap
1032 program, which minimized the effects on the deconvolution process and resulted in very good
1033 fits to these data (Figure 2). The uncertainties on the A- and B-centers concentrations were
1034 determined to be <5%. This was achieved by increasing and decreasing the amount of IaA and

IaB that are subtracted until a clear peak or a ‘negative’ peak were observed at 1282 cm⁻¹ (A-centers) and 1332 cm⁻¹ (B-centers). After baseline correction and subtraction of both diamond and nitrogen bands, the concentrations of water and carbonate (Table 2) were determined using the maximum absorbance of water and carbonate and their absorption coefficients (Weiss et al., 2010). These concentrations were used to calculate the carbonate mole fraction (CMF) of the trapped fluids (CMF=carbonate/(water+carbonate) molar ratio). Absorption peaks, known to be caused by primary mineral microinclusions trapped by the diamond during its growth, as well as daughter mineral phases that grew from the trapped HDFs within the microinclusions, were documented and used to confirm the general characteristics of the host rock mineralogy and the nature of the diamond-forming fluids.

Cathodoluminescence (CL) imaging and Electron probe microanalyzer (EPMA) analyses

Cathodoluminescence imaging (total intensity at 400–700 nm) of the diamonds was recorded using a Gatan MiniCL attached to a JEOL JXA 8600 EPMA at the Institute of Earth Sciences, HUJI. The acceleration voltage was 25 kV and the beam current was 75 nA. These images provide the internal structure of the diamond and allow the determination of the exact location of the microinclusions relative to the growth history of the diamond (Figure 1 and Supplementary Figure S1).

The major element compositions of the microinclusions were determined using a JEOL JXA 8600 EPMA equipped with a Pioneer-Norvar EDS (133 eV) detector at the Institute of Earth Sciences, HUJI. Backscattered electron imaging was used to detect shallow, subsurface microinclusions (<2 µm depth). Each inclusion was analyzed for 100 s using an acceleration voltage of 15 kV and a beam current of 10 nA. The spectral data were reduced using the ZAF/PROZA correction procedure software supplied by Noran (Bastin and Heijligers, 1991).

The total amount of oxides and Cl in each analysis varied between 1.2 and 29 wt.% with an average of 7.7 wt.% for all 347 analyzed HDF microinclusions and between 1.9 and 61 wt.% with an average of 14 wt.% for 190 analyzed mineral microinclusions (Supplementary Table A, B). The low and variable sums reflect the small size of the inclusions, their depth and their high content of undetected water and carbonates. Precision approximately follows: 2σ (%) = 2/oxide in wt.% (Jablon and Navon, 2016), and is <20% for oxide concentrations of 0.05 wt%, <10% for 0.25 wt%, <6% for 0.5 wt% and <2% for 1 wt%. The ZAF/PROZA processing assumed that the difference from 100 wt.% is comprised of pure carbon. Later, all oxide and chlorine concentrations were normalized to 100 wt.% on a carbon-free and volatiles-free basis (where Cl is present, excess calculated oxygen leads to a normalized total of more than 100%) and the average composition of the HDF in the diamond was calculated.

Laser ablation ICP-MS analyses

Trace element concentrations were determined using a Quantel Brilliant 266 nm Nd:YAG pulsed laser with a beam diameter of 100 μm coupled to an Agilent 7500 ICP-MS at GEMOC, Macquarie University, NSW, Australia. Background was measured for 100 s followed by 130 s of diamond ablation. Data were reduced using the GLITTER 4.4 software. A doped cellulose external standard and the diamond carbon were used as internal standards (Rege et al., 2010; Rege et al., 2005). Only the most homogeneous and stable portions of the time-resolved signals were selected for each diamond. For the high impurity content of the diamond, blank corrections (Rege et al., 2005 Table S3) are less than 1–2%, except for Ca where it is equivalent to 12 ± 5 ppm or 10% of the typical measured concentrations. The method limit of detection (LOD) is defined as 3.25 times the uncertainty on the background counts and the limit of quantitation (LOQ) is defined as 10 times the uncertainty on the background (Rege et al., 2010). The

precision (expressed as %rsd) is 10% for concentrations between 1 and 100 ppm, 20% for 0.1–1 ppm, 30% for 0.01–0.1 ppm and 40% for values <0.01 ppm. These analyses yield the concentrations of elements in the diamond host. In order to obtain the trace element concentrations of the trapped fluids, all values were corrected to the average K content of the microinclusions of each diamond as measured by EPMA (on water+carbonate free basis).

1086

1087 **Additional references**

1088 Bastin, G., Heijligers, J., 1991. Electron Probe Quantitation, in: Heinrich, K., Newbury, D. (Ed.),
1089 Workshop at the National Bureau of Standards, Gaithersburg, Maryland. Plenum Press, New
1090 York, pp. 145-161.

1091 Boyd, S.R., Kiflawi, I., Woods, G.S., 1994. The relationship between infrared-absorption and the
1092 A defect concentration in diamonds. *Philos. Mag. B-Phys. Condens. Matter Stat. Mech.*
1093 *Electron. Opt. Magn. Prop.* 69, 1149-1153.

1094 Boyd, S.R., Kiflawi, I., Woods, G.S., 1995. Infrared-absorption by the B-nitrogen aggregate in
1095 diamond. *Philos. Mag. B-Phys. Condens. Matter Stat. Mech. Electron. Opt. Magn. Prop.* 72,
1096 351-361.

1097 Howell, D., O'Neill, C.J., Grant, K.J., Griffin, W.L., Pearson, N.J., O'Reilly, S.Y., 2012. mu-
1098 FTIR mapping: Distribution of impurities in different types of diamond growth. *Diamond*
1099 *and Related Materials* 29, 29-36.

1100 Jablon, B.M., Navon, O., 2016. Most diamonds were created equal. *Earth and Planetary Science*
1101 *Letters* 443, 41-47.

1102 Kiflawi, I., Mayer, A.E., Spear, P.M., Vanwyk, J.A., Woods, G.S., 1994. Infraren-absorption by
1103 the single nitrogen and A defect centers in diamond. *Philos. Mag. B-Phys. Condens. Matter*
1104 *Stat. Mech. Electron. Opt. Magn. Prop.* 69, 1141-1147.

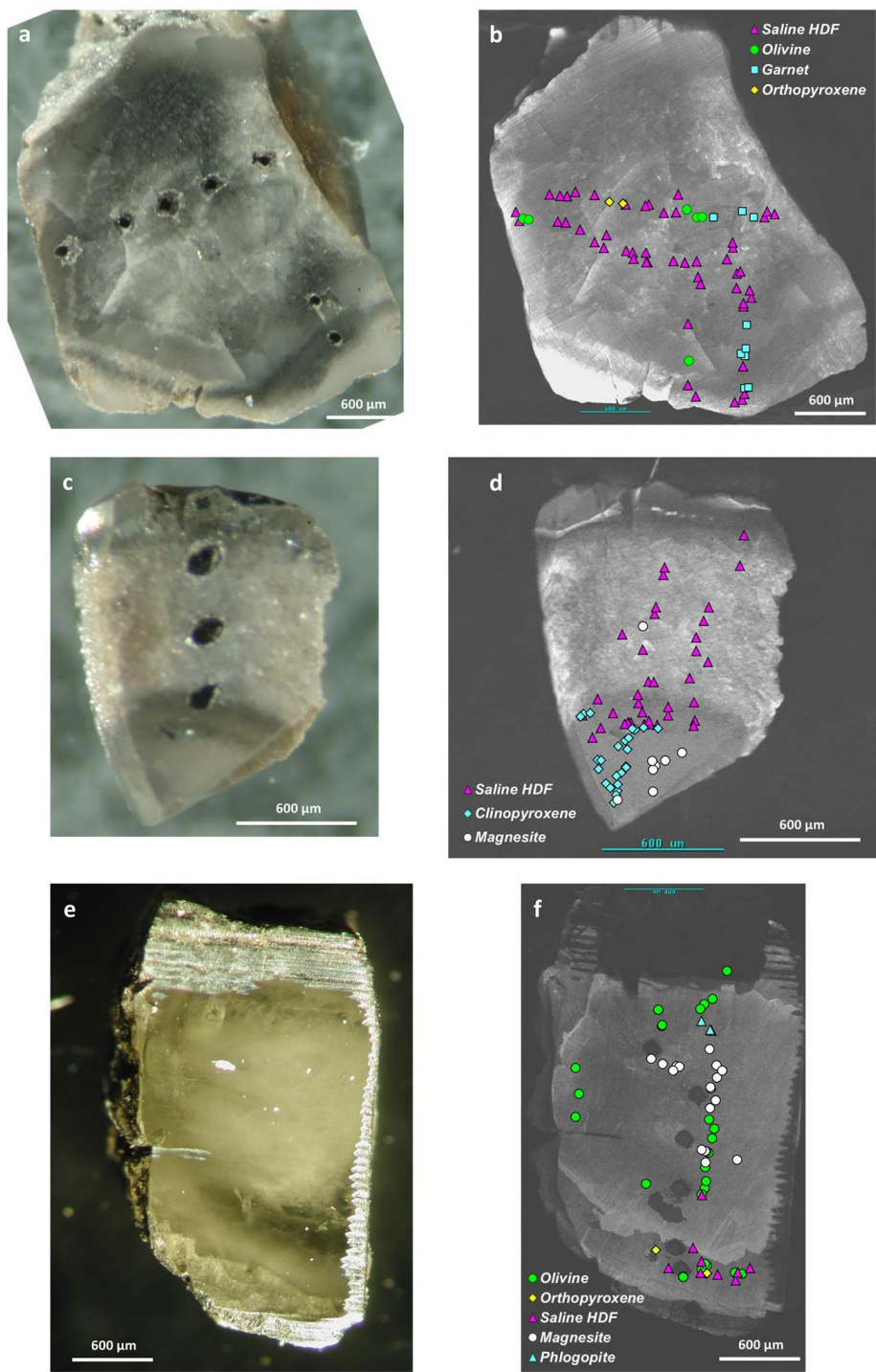
1105 Rege, S., Griffin, W.L., Pearson, N.J., Araujo, D., Zedgenizov, D., O'Reilly, S.Y., 2010. Trace-
1106 element patterns of fibrous and monocrystalline diamonds: Insights into mantle fluids. *Lithos*
1107 118, 313-337.

1108 Rege, S., Jackson, S., Griffin, W.L., Davies, R.M., Pearson, N.J., O'Reilly, S.Y., 2005.
1109 Quantitative trace-element analysis of diamond by laser ablation inductively coupled plasma
1110 mass spectrometry. *Journal of Analytical Atomic Spectrometry* 20, 601-611.

1111 Weiss, Y., Kiflawi, I., Navon, O., 2010. IR spectroscopy: Quantitative determination of the
1112 mineralogy and bulk composition of fluid microinclusions in diamonds. *Chemical Geology*
1113 275, 26-34.

1114 Zaitsev, A. M., 2001. *Optical Properties of Diamond. Handbook*, 502 pp.

1115



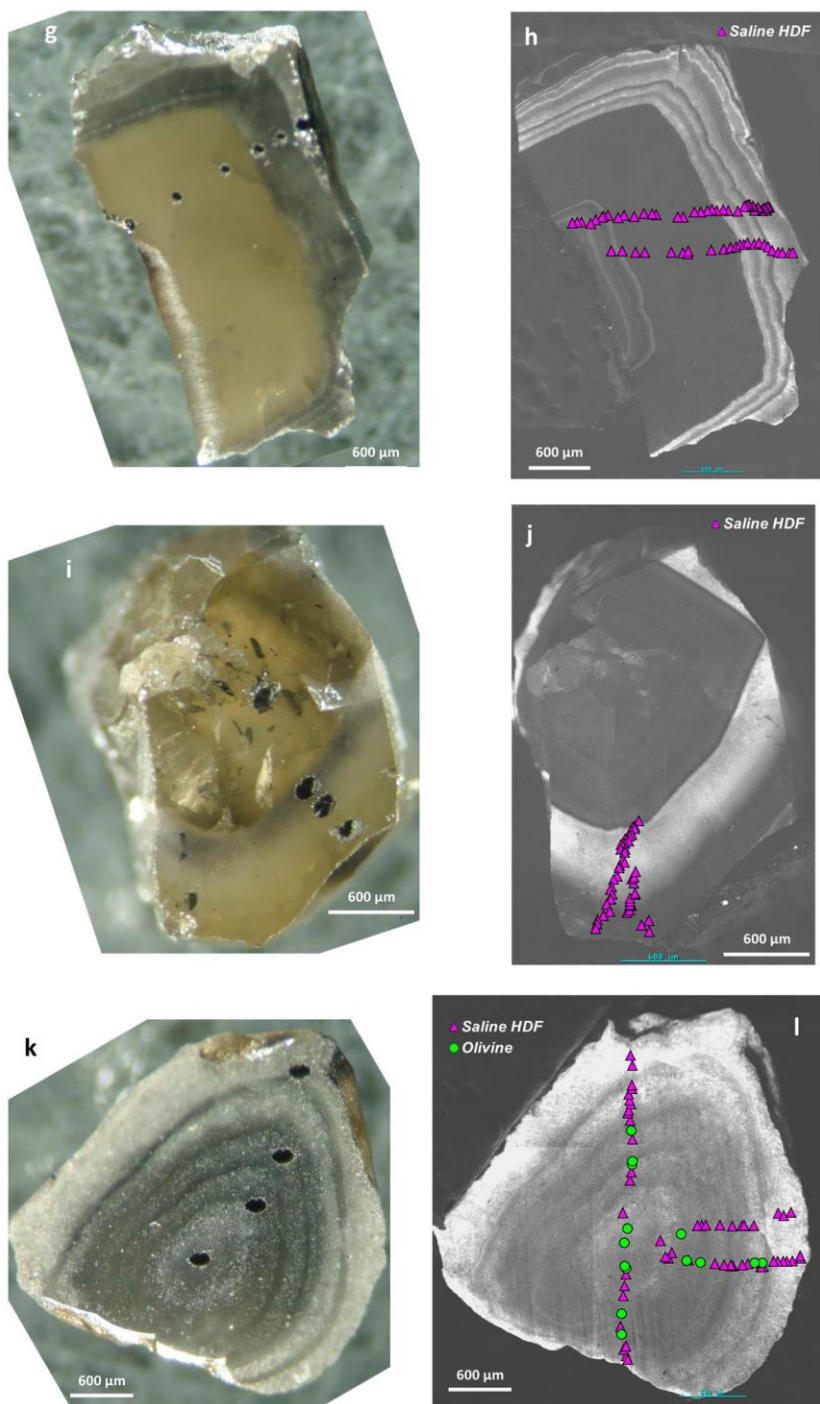
1116

1117

1118

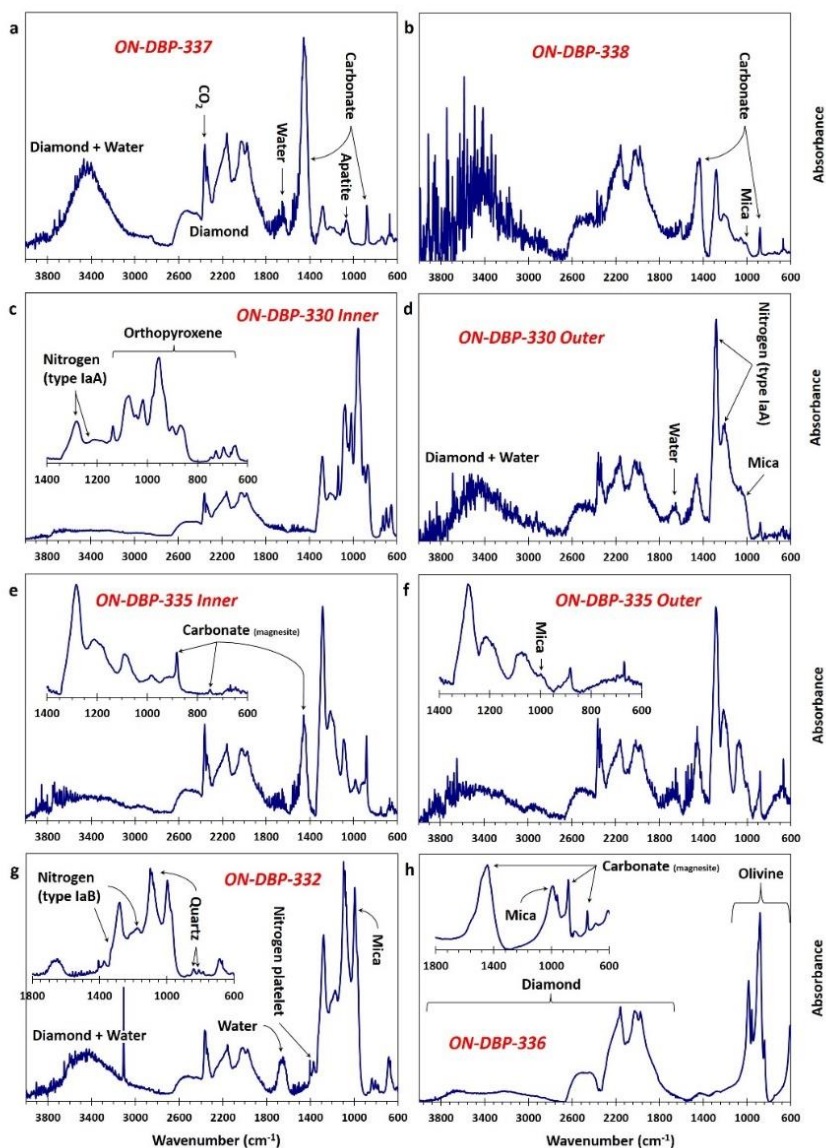
Supplementary Figure S1: Photomicrograph and Cathodoluminescence (CL) images of microinclusion-bearing diamonds from the DeBeers-Pool kimberlites. (a) and (b) Diamond ON-DBP-331; (c) and (d) Diamond ON-DBP-335; (e) and (f) Diamond ON-DBP-336; (g) and (h) Diamond ON-

1119 DBP-337; (i) and (j) Diamond ON-DBP-338; (k) and (l) Diamond ON-DBP-339. The location and type (i.e. mineral or HDF) of the microinclusions
 1120 that were analyzed by EPMA in each diamond is superimposed on its CL image. Pits were excavated during laser ablation ICP-MS analysis.



1121
 1122 **Supplementary Figure S1 (continued):** Photomicrograph and Cathodoluminescence (CL) images of microinclusion-bearing diamonds from the
 1123 DeBeers-Pool kimberlites. (a) and (b) Diamond ON-DBP-331; (c) and (d) Diamond ON-DBP-335; (e) and (f) Diamond ON-DBP-336; (g) and (h)
 1124 Diamond ON-DBP-337; (i) and (j) Diamond ON-DBP-338; (k) and (l) Diamond ON-DBP-339. The location and type (i.e. mineral or HDF) of the

microinclusions that were analyzed by EPMA in each diamond is superimposed on its CL image. Pits were excavated during laser ablation ICP-MS analysis.



Supplementary Figure S2: Original infrared absorbance spectra of six different diamonds from DeBeers-Pool kimberlites (a-h). The intrinsic diamond bands at 1800–3800 cm⁻¹, without CO₂ and water overlapping absorbance, is best shown in (h). Nitrogen-related substitutions in the diamond lattice show absorbance in the range of 1150–1400 cm⁻¹; diamonds ON-DBP-330, 335, 337, 338 (a-f) show nitrogen absorbance due to A-centers only (Type IaA spectrum); diamond ON-DBP-332 (g) show absorbance of both A- and B-centers (Type IaB spectrum) and nitrogen platelets peak; diamond ON-DBP-336 (h) is a type IIb diamond, carrying no nitrogen impurities. Absorbance due to mineral microinclusions and daughter phases within HDF microinclusions are also observed: bands at ~1450 and ~880 and ~750 cm⁻¹ are typical of carbonate absorption. The broad band at ~3440 cm⁻¹ and the peak at ~1650 are due to the presence of liquid water. Mica main peak is observed at ~1000 cm⁻¹. Apatite main peak is at 1065 cm⁻¹ and has two additional peaks at 1060 and 605 cm⁻¹. Quartz main peak is at 1092 cm⁻¹, and has two small characteristic peaks at ~810 and ~785 cm⁻¹. Multiple peaks of olivine and pyroxene were also identified between 600–1150 cm⁻¹. The inset in (c-g) shows in detail the absorbance range between 600–1800 cm⁻¹ of the full spectrum presented. The inset in (h) represents absorbance in

1138 the range between 600–1800 cm^{-1} of a spectrum taken at the inner part of diamond ON-DBP-336, while the full spectrum represents
1139 absorbance at the outer part of this diamond, differences are due to different mineral microinclusions characteristics in the inner and outer
1140 parts of this diamond (see also supplementary Figure S1).